ALMA high-frequency long-baseline campaign in 2017: an investigation of phase-referencing cycle times and effective baseline lengths using band-to-band and in-band phase calibration techniques

Maud, L.T.; Asaki, Y.; Dent, W.R.F.; Hirota, A.; Fomalont, E.B.; Takahashi, S.; ... ; Carpenter, J.

The Astrophysical Journal Supplement Series, 259:10 (25pp), 2022 March https://doi.org/10.3847/1538-4365/ac3b57

ALMA High-frequency Long-baseline Campaign in 2017: An Investigation of Phase-referencing Cycle Times and Effective Baseline Lengths Using Band-to-band and In-band Phase Calibration Techniques

Luke T. Maud[1,2], Yoshiharu Asaki[3,4,5], William R. F. Dent[3], Akihiko Hirota[3,4], Edward B. Fomalont[3,6], Satoko Takahashi[3,4,5], Satoki Matsushita[7], Neil M. Phillips[1], Tsuyoshi Sawada[3,4], Stuartt Corder[3], and John Carpenter[3]
[1] ESO Headquarters, Karl-Schwarzchild-Str 2, D-85748 Garching, Germany; lmaud@eso.org
[2] Allegro, Leiden Observatory, Leiden University, PO Box 9513, 2300 RA Leiden, The Netherlands
[3] Joint ALMA Observatory, Alonso de Córdova 3107, Vitacura, Santiago, 763 0355, Chile
[4] National Astronomical Observatory of Japan, Alonso de Córdova 3788, Office 61B, Vitacura, Santiago, Chile
[5] Department of Astronomical Science, School of Physical Sciences, The Graduate University for Advanced Studies (SOKENDAI), 2-21-1 Osawa, Mitaka, Tokyo 181-8588, Japan
[6] National Radio Astronomy Observatory, Edgemont Road, Charlottesville, VA 22903, USA
[7] Academia Sinica Institute of Astronomy and Astrophysics (ASIAA), 11F Astronomy-Mathematics Building, AS/NTU, No.1, Sec. 4, Roosevelt Road, Taipei 10617, Taiwan, R.O.C.
Received 2021 October 1; revised 2021 November 10; accepted 2021 November 17; published 2022 February 23

Abstract

The Atacama Large Millimeter/submillimeter Array can achieve unprecedented spatial resolutions of 15 to 5 mas with the longest baselines of 16 km and observing at the highest frequencies of 275–950 GHz (1.09–0.30 mm). Two conditions are paramount for successful observations at these frequencies: a phase calibrator in close proximity to the science target and a stable-enough atmosphere to provide a low residual phase rms post-phase-referencing. We investigate the effect of phase-referencing cycle times, for in-band and band-to-band (B2B) observing techniques, using close and distant phase calibrators, at bands 7, 8, and 9 for baselines >2000 m. We find that (1) the phase rms estimated from baselines longer than the effective baseline increases as a function of $\sqrt{\text{time}}$. (2) The expected coherence estimated using the expected phase rms corresponds well to the achieved image coherence. (3) Faster phase-referencing cycle times (<1 minute) improve phase calibration accuracy and image coherence when close phase calibrators (<2°) are used. (4) For cycle times <2 minutes the negative impact of distant phase calibrators dominates the phase error budget. We also explore whether a theoretical parameterization of the effective baseline used to estimate the phase rms and a phase stability measurement, combined with an empirical parameterization of coherence degradation as a function of calibrator separation, is suitable in estimating the expected coherence of target images. The latter proves to be more accurate. Finally, we illustrate a pragmatic approach in establishing an optimal observing strategy via dynamic cycle times and on-calibrator scan lengths.

Unified Astronomy Thesaurus concepts: Atmospheric effects (113); Long baseline interferometry (932); Submillimeter astronomy (1647); Phase error (1220)

1. Introduction

Long-baseline observations (∼16 km) with the Atacama Large Millimeter/submillimeter Array (ALMA) are able to achieve unprecedented angular resolutions at submillimeter wavelengths. It is the only submillimeter interferometer that regularly observes at frequencies >450 GHz (wavelengths <0.7 mm). ALMA long-baseline observations were showcased in ALMA Partnership et al. (2015a, 2015b, 2015c) and since 2015, ALMA has been observing with long baselines in bands 3, 4, and 6, and in band 5 shortly after. In Cycle 7, band 7 long baselines have also been offered for use. Theoretically, ALMA can reach an angular resolution of 5 mas at the highest observable frequency of 950 GHz (ALMA band 10). Such observations are extremely challenging. First, Earth's atmosphere causes irreversible signal loss, due to attenuation primarily from water vapor. Thus, the precipitable water vapor (PWV) content must be limited. Depending on the exact frequency tuning, ALMA generally imposes PWV limits of ∼0.472 and ∼0.658 mm at bands 10 and 9, respectively. On the Chatantor plateau where ALMA is located, these occur around ∼20%–25% of the time in the best weather months, July and August. The PWV can be measured easily and thus observations are easy to limit to the correct conditions. Perhaps more important, like all synthesis arrays, imaging for ALMA can only take place when there are coherent signals between all pairs of antennas in an array, i.e., the baselines. Turbulent atmospheric cells cause fluctuations of path-length delays as a function of position and time in the signals to each antenna in the baselines, which then cause signal decorrelation. Such decorrelation will lead to a loss in sensitivity, negatively affect the accuracy of amplitude calibrations, and if the path-length delays are large enough (tens of degrees of phase), will cause imaging defects.

The estimated coherence[8] for the interferometric visibilities ($\boldsymbol{V} = \boldsymbol{V}_0 e^{i\phi}$, where $\boldsymbol{V}_0$ represents the true visibilities and ϕ are the phase fluctuations caused by the troposphere; Thompson et al. 2017) can be calculated using

$$\langle \boldsymbol{V} \rangle = \langle \boldsymbol{V}_0 \rangle \langle e^{i\phi} \rangle = \langle \boldsymbol{V}_0 \rangle e^{-\sigma_\phi^2/2}, \quad (1)$$

[8] We use this term throughout the paper to denote the coherence value estimated from Equation (1) when inputting a measured phase rms fluctuation and $\boldsymbol{V}_0 = 1$; see also Bulter et al. (2001).

if we assume Gaussian random phase fluctuations, ϕ, with an rms of σ_ϕ (in radians) and a zero degree mean phase (Thompson et al. 2017). One can establish σ_ϕ (radians) directly from the variability of the path-length delays (ℓ, in microns) introduced by the changing atmosphere for a given observing frequency ($\nu_{\rm obs}$, in hertz) from

$$\sigma_\phi = 2\pi\ell\,\frac{\nu_{\rm obs}}{c} \quad \text{(radians)}, \tag{2}$$

where c is the speed of light (in μm s^{-1}). Thus, with increasing observing frequency, regardless of baseline length, the phase rms will increase linearly.[9]

The characteristics of atmospheric phase fluctuations, as seen by an interferometer, can be explained using the spatial-structure function (SSF) $D_\phi(b)$. The SSF is the dispersion of the atmospheric phase as a function of baseline length b (see also Tatarski et al. 1961; Wright 1996; Carilli & Holdaway 1999; Matsushita et al. 2017) and is related to the phase rms by $\sigma_\phi = \sqrt{D_\phi(b)}$, where

$$D_\phi(b) = \langle(\phi(x+b) - \phi(x))^2\rangle, \tag{3}$$

such that $(\phi(x+b) - \phi(x))$ is the phase difference between the two antennas, located at $x+b$ and x, respectively, and hence b is the baseline length. Measurements by Matsushita et al. (2017) indicated that, in general for ALMA, σ_ϕ increases as $b^{0.60}$–$b^{0.65}$ for baselines $b < 1$ km and as $b^{0.17}$–$b^{0.31}$ for $b > 1$ km (see also ALMA Partnership et al. 2015d), closely following Kolmogorov turbulence theory with powers 0.83 and 0.33, for three-dimensional (3D) and two-dimensional (2D) turbulence, respectively (see also Coulman 1990; Sramek 1990; Wright 1996; Carilli & Holdaway 1999). In terms of atmospheric studies, the break between the 3D and 2D scales points to the height of the turbulent layer (e.g., Lay 1997), which is typically between 500 m and 1 km for ALMA. Notably, Matsushita et al. (2017) identified rare cases, usually in low PWV conditions, where a break in the SSF did not occur and the scaling power remains steeper (∼0.5–0.6).

Under the premise of a frozen flow of the turbulent atmospheric screen (Taylor 1938), the temporal-structure function (TSF) $\bar{D}_\phi(t)$, which represents the phase fluctuations at a single position over a time interval, t, can be tied to the SSF for a given baseline length via $b = vt$, $\bar{D}_\phi(t) = D_\phi(b)|_{b=vt}$ (see also Asaki et al. 1996). For Kolmogorov turbulent cells, phase fluctuations for a given baseline will increase up to a point defined as a crossing time (also known as the corner time), t_c, beyond which both antennas making up the baseline will see the same common turbulent cell (Thompson et al. 2017). Smaller baselines do not sample the large-scale turbulent cells that contain the most power and saturate quickly after shorter t_c, whereas longer baselines see larger cells (up to scales comparable with the baseline length) and consequently have longer crossing times. Importantly, if one samples phase changes faster than t_c for any given baseline and uses these as phase calibration solutions, the subsequently calibrated data would have phase variations equivalent to those of shorter baselines. For interferometric phase referencing, a calibrator is visited interleaved with target observations over a timescale of a cycle time $t_{\rm cyc}$, which encompasses a full target scan, a full calibrator scan, and twice the slew time moving between sources. Holdaway & Owen (1995) report for phase referencing that a relevant timescale would be $t_{\rm cyc}/2$, understood as the phase variation occurring over half a cycle time being the most in error (see Section 4.1). The same relevant timescale is also reported by Carilli & Holdaway (1999) with reference to self-calibrated data calibrated over a specific averaging time (replacing $t_{\rm cyc}$ with $t_{\rm ave}$), where the factor of 2 arises from the mean calibration applying to the middle of a solution interval. After phase calibration with a cycle time, $t_{\rm cyc}$, the remaining baseline-based phase rms is therefore thought to be parameterized as $\sigma_\phi = \sqrt{D_\phi(v_{\rm wind}t_{\rm cyc}/2 + d)}$, where d is the is the geometrical distance between the lines of sight to the target and the phase calibrator at the altitude of the turbulent layer, $v_{\rm wind}$, is a reasonable proxy for the atmospheric screen speed (Holdaway 1992; Holdaway & Owen 1995; Holdaway et al. 2004; Thompson et al. 2017)[10], D_ϕ is the aforementioned SSF, and where $v_{\rm wind}t_{\rm cyc}/2 + d$ can be considered as the calculated effective baseline length $B_{\rm eff,calc}$. Following this parameterization, the phase rms should remain constant for all baselines $> B_{\rm eff,calc}$ after phase referencing.

Provided there is a close and strong-enough calibrator (e.g., Maud et al. 2020), more regular calibrator visits, using fast-switching phase referencing, should therefore be able to notably reduce the remaining phase rms that usually hinders accurate long-baseline observations. The theory (e.g., Holdaway & Owen 1995; Woody et al. 1995; Lay 1997) is supported by observations using the Very Large Array (VLA) (Carilli & Holdaway 1997, 1999), the Nobeyama Millimeter Array (NMA) (Morita et al. 2000), the Submillimeter Array (SMA) (Lal et al. 2007) and more recently, using ALMA (Asaki et al. 2014, 2016), where phase-referencing cycle times as short as ∼20 s were realized. Indeed, ALMA was designed with fast switching in mind (Rampini et al. 2010; Mangum et al. 2006).

Maud et al. (2020) noted that for high-frequency long-baseline ALMA observations (>450 GHz, >5 km) the water-vapor-radiometer (WVR) system employed at ALMA will provide a negligible phase correction, as there is little PWV content (see also Maud et al. 2017) and so phase referencing using fast switching must be relied upon. The main problem is that high-frequency quasars, acting as phase calibrators, are often much weaker due to their intrinsic spectral index and therefore need longer integration times to achieve a sufficient signal-to-noise ratio (S/N) for generating phase solutions. This is compounded by higher receiver temperatures and a higher sky noise, leading to higher system temperatures ($T_{\rm sys}$) compared to lower frequencies. Long integration times circumvent the ability to use fast-switching calibration where calibrator scans should last <10 s in duration. Asaki et al. (2020a) calculated that the mean angular separation of a calibrator from a target at band 10 is 12°.6 after examining the ALMA calibrator catalog when considering fast-switching requirements (8 s integration time and a total bandwidth of 15 GHz). Therefore, considering the absolute need for a calibrator <4°–5° away for band 7 long baselines and potentially even closer for higher frequencies (Maud et al. 2020), it is very unlikely that long-baseline band 10 observations would be possible. The foreseeable way to realize short integration times with high S/N is to observe calibrators at a lower frequency where they are naturally much stronger and more likely to be closely located with

[9] Dispersion can occur near strong atmospheric absorption lines, which is nonlinear.

[10] Depending on which simulation, or study, the factor of 2 is absent or multiplicative. Also see Y. Asaki (2022, in preparation).

respect to any given target. The method of transferring phase solutions from low to high frequencies at ALMA is called Band-to-Band (B2B) phase transfer (see Asaki et al. 2020a, 2020b; Maud et al. 2020 for more details).

In this paper, as part of the series on the High-Frequency Long-Baseline-Campaign undertaken during 2017 (HF-LBC-2017; see also Asaki et al. 2020a, 2020b; Maud et al. 2020), we make comparisons of the effect of phase-referencing cycle times using both B2B and the standard in-band phase calibration techniques. These comparisons are part of the stage 3 tests enumerated in Asaki et al. (2020a). For stage 3 there are three main goals of the observations:

1. To make a direct comparison between the standard, in-band, phase referencing, and B2B phase referencing.
2. To investigate the detrimental effect on calibration due to increased phase calibrator to target separation angles.
3. To test a variety of phase-referencing cycle times from $\sim$120 s down to the effective ALMA fast-switching limit of 24 s.

Goals (1) and (2) are detailed in Maud et al. (2020), which focused specifically on the effect of phase calibrator separation angles when using only fast switching, while in this work we will examine the effect of cycle times, goal (3). In addition we examine both (i) the theoretical parameterization of the effective baseline length and (ii) a method combining a phase stability observation with an empirical parameterization of coherence loss with calibrator separation angle to estimate the likely coherence achievable in images. We use our finding to suggest a possible approach to optimize ALMA observations.

In Section 2 we provide a brief recap of the observational tests, the data reduction and the methodology used for the analysis. In Section 3 we detail the results of our goal (3) investigations for both the B2B and in-band calibration techniques and in addition, consider differences due to calibrator separation angle. In Section 4 we conduct additional analysis on effective baseline lengths, investigate how to estimate the image coherence, and present a possible method on how to select the most optimal cycle time. Finally, in Section 5 we provide a brief summary.

2. Observations, Reduction, and Methodology

We detail thoroughly the observations, their reduction, and our imaging and assessment methodology in Maud et al. (2020). We provide a shortened overview here.

The experiments were made as part of the 2017 high-frequency and long-baseline campaign HF-LBC-2017 (Asaki et al. 2020a) toward the end of Cycle 4 (2017 June to October). We conducted 50 full-length observations, of which 44 were used in our analysis.[11] The observations were spread over a number of months, thus covering maximal baseline lengths from $\sim$1.5 to $\sim$15 km, and a variety of PWV conditions and phase stability conditions. The tests were slotted into observing time gaps or when the numbers of antennas were limited, thus we have a range of antennas, between 13 and 40, for each observation. Strict phase rms limits were not employed as that would have only selected stable conditions. Our data can therefore have phase rms values much higher than would be acceptable for PI science at such frequencies, this also being our aim, such that we can study the effect of changing cycle times in a range of stability conditions.

Each of our observations was conducted in a sequence of six blocks: a strong quasar for Differential-Gain-Calibration (DGC; Asaki et al. 2020a; Maud et al. 2020), followed by a phase calibrator and target block using in-band phase referencing, continued by a B2B phase calibrator and target referencing block, one repeat of the in-band block, one repeat of the B2B block, and then a final DGC block. In Figure 1 we illustrate the sequence and identify the blocks making up the observation—this figure is reproduced from Maud et al. (2020). An entire observing sequence is around 50 minutes in length, including all required $T_{\rm sys}$ and pointing calibrations and delays between the blocks. The target on-source duration is $\sim$2 minutes for both the in-band or B2B observing blocks, thus a total of $\sim$4 minutes on source for each of the in-band and B2B observations, respectively. Table 1 gives the overview of the analyzed experiments, the baseline ranges, times of day, and frequency pairings. A key point of these tests was that all B2B blocks use a phase calibrator to target separation $<2^\circ$ to mimic the likely cases when B2B would be employed given that phase calibrators at the low frequency will be more easily found closer to the science target. In the in-band blocks, either the same calibrators chosen for the B2B block or one more distant, between $\sim2^\circ$ and 11° away from the target, is used.

2.1. Data Reduction, Processing, and Imaging

The in-band observations were calibrated according to standard calibration practices used for ALMA quality-assurance reduction (called QA2, Petry et al. 2020), i.e., making WVR, $T_{\rm sys}$, and antenna position corrections, followed by bandpass, phase, and amplitude correction. We used a slightly modified script to identify sources and spectral windows (SPWs) unique to our testing data. Flagging was performed conservatively in line with normal science observations in that we avoided flagging the target except in the most egregious cases. For B2B calibration, additional steps were added to derive the DGC solution and in subsequent phase calibration steps that scale the low-frequency (ν_l) phase calibrator solutions to the high-frequency (ν_h) target by the ratio between frequencies, ν_h/ν_l. The interpolation and scaling use the "linearPD" option in the APPLYCAL task within CASA (McMullin et al. 2007). Maud et al. (2020) provide a more detailed description of the procedure.

In order to address goal (3), the topic of this paper, we calibrate the data using the native observing cycle time of $\sim$24 s and also by additionally culling phase calibrator scans to artificially create longer cycle times of 48, 72, 96, and 120 s. Images for both in-band and B2B were then made using only the scans that were calibrated by a bracketing phase calibrator scan, as culling some calibrator scans often rendered a missing phase calibrator at the end of the observations. Furthermore, because the targets are point-source quasars, we also perform self-calibration in order to have an "ideal" calibration to compare both the in-band and B2B calibration with. For self-calibration we use the integration timescale (int) $\sim$1 s where possible for strong- enough sources; however, for some data sets the scan timescale of $\sim$9 s was used to improve the S/N of the solutions (Cornwell & Wilkinson 1981; Brogan et al. 2018). Following from the detailed assessment of many imaging parameters in Maud et al. (2020), we focus here only

[11] One band 10 test and four band 9 tests failed due to source nondetection as a result of high image noise, while one band 7 could not be calibrated due to missing observing blocks.

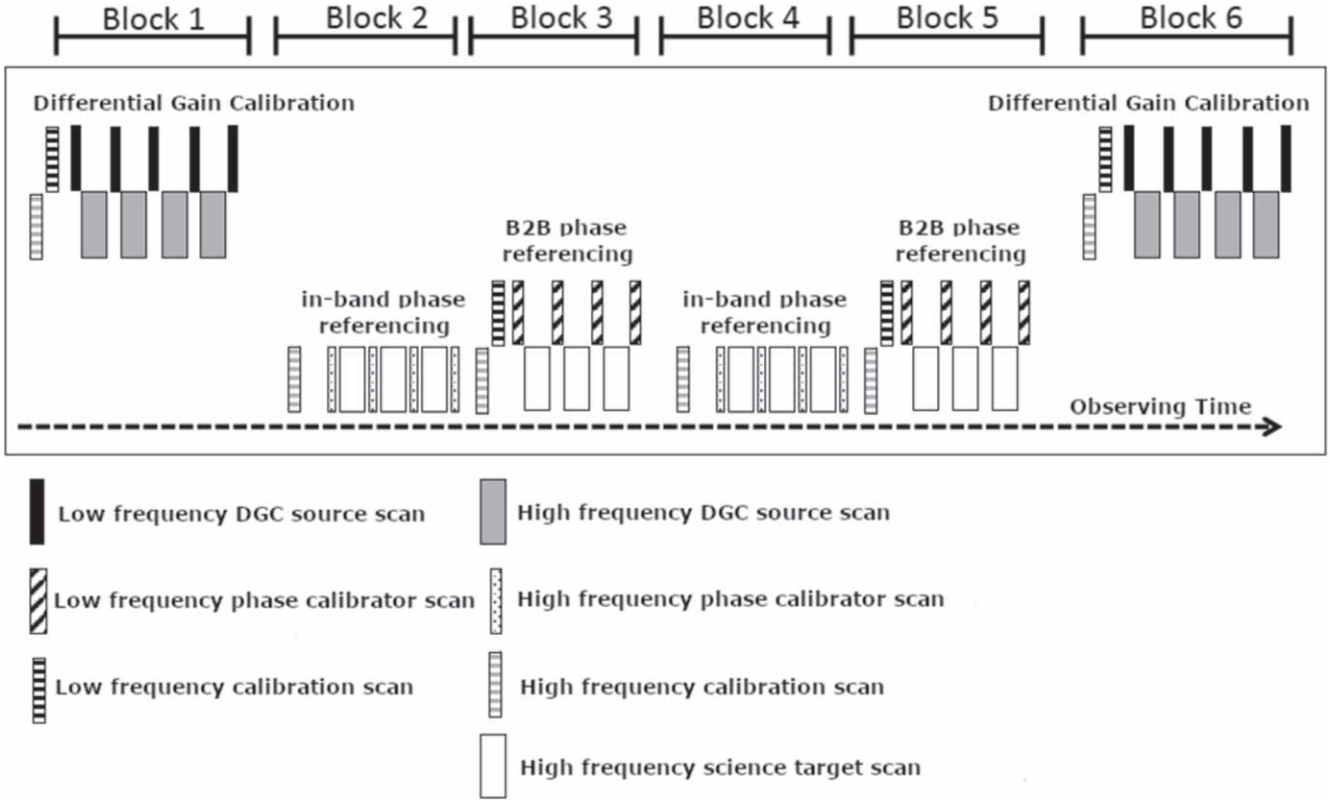

Figure 1. The full observing sequence for an entire B2B and in-band test observation. One full observation is made of six blocks, divided up into the first DGC observation, in-band referencing, B2B referencing, the second in-band block, the second B2B block, and finally, the ending DGC block. The figure is illustrative and not accurate in terms of observing time per scan or the number of scans. Scan lengths in our observations are 9 s for all targets, regardless of observing at the high or low frequency. The individual scans are identified in the key to the bottom. This figure is reproduced from Maud et al. (2020).

on the image coherence (this is also referred to as the fractional peak flux recovered, e.g., Dodson & Rioja 2009; Martí-Vidal et al. 2010a; Rioja & Dodson 2011; Rioja et al. 2015) in order to make comparisons with cycle times and phase rms measures for different calibration techniques.

The imaging is undertaken in an automatic fashion using the CLEAN command in CASA. Square maps with sizes of 512×512 or 1024×1024 pixel are used dependent on resolution, while pixel sizes are chosen to be 5 times smaller than the synthesized beam (band 9 uses 7 times smaller ones). We used Briggs weighting with a robust parameter of 0.5 (Briggs 1995). Cleaning uses a circular region of 15 pixel radius in the center of the map using a fixed number of 50 iterations. The peak and integrated flux density are measured within this aperture, whereas the map noise is taken within an annulus outside this and extending to 250 or 500 pixels in radius for image sizes of 512 or 1024 pixels, respectively. The same assessment is made for the self-calibrated images.

2.2. Measuring the Phase Stability

Our main measure of phase stability is what we term the expected phase rms, and is a function of time. We calculate this using the bright DGC source and after application of the WVR solutions but otherwise without any additional calibration. We use a similar metric to the SSF but specifically impose a temporal component in order to understand the effect of timescales:

$$\sigma_\phi(b, t) = \sqrt{D_\phi(b, t)} = \left\langle (\phi(x + b) - \phi(x))^2 \right\rangle_t^{1/2} (\mathrm{deg}), \quad (4)$$

where, different from Equation (3), we average over the timescale t (this approaches the traditional SSF in the limit $t = t_{\mathrm{obs}}$—the total observation duration). The expected phase rms is representative of the phase variations that remain in the data after ideal phase referencing (e.g., Maud et al. 2020), because the action of phase referencing should remove fluctuations longer than the cycle time, and hence variations $\lesssim t_{\mathrm{cyc}}$ remain largely unchanged. We explore this further in Section 3.2. To reiterate, the expected phase rms measure is used as the proxy of the phase rms we would expect any target source to have after WVR correction and due solely to atmosphere variations occurring over a timescale t which would remain after phase referencing with a cycle time, $t_{\mathrm{cyc}} = t$.

In calculating the expected phase rms from the DGC source we use only the low-frequency scans to maximize the S/N. Given the fixed and repetitive scan lengths, if we exclude the high-frequency scan in between selected consecutive low-frequency scans, we can measure the expected phase rms[12] over a range of timescales. Selecting every two, four, and six consecutive low-frequency scans, considering the frequency-switching times and the gap for the high-frequency scan, we measure timescales of ∼33, 81, and 129 s, which provide reasonable coverage of the data calibration cycle times, 24, 48, 72, 96, and 120 s (see Section 3.1). In addition, we measure the residual phase rms, which is extracted from the DGC

[12] For these phase rms calculations, we account for the mean phase in the scans selected and we use only WVR corrected data. A standard deviation calculation for the DGC scan pairings is therefore used rather than a true rms statistic.

Table 1
Overview and Parameters of the 44 Analyzed In-band–B2B Observations Conducted as Part of HF-LBC-2017

Name	Date	Time (UTC)	DGC source				No. Ants	PWV (mm)	Wind Speed (m s^{-1})	Maximum Baseline (m)
			Name	Flux (Jy)	α	El. (deg)				
Band 7-3										
J2228-170827-B73-1deg	2017-08-27	04:48:24	J2253+1608	5.89	−0.705	50.6	48	0.62	6.0	4540
J2228-170829-B73-1deg	2017-08-29	07:33:25	J2253+1608	5.89	−0.705	34.6	48	1.45	7.4	4734
J2228-170829-B73-3deg	2017-08-29	02:07:47	J2253+1608	5.89	−0.705	33.5	47	1.33	7.0	5049
J2228-170829-B73-6deg	2017-08-29	02:57:20	J2253+1608	5.89	−0.705	41.4	47	1.28	6.5	4874
J0449-170829-B73-2deg	2017-08-29	08:24:35	J0522−3627	4.44	−0.311	49.6	48	1.57	6.4	4798
J0449-170829-B73-3deg	2017-08-29	09:21:55	J0522−3627	4.44	−0.311	60.9	48	1.70	5.5	4807
J2228-170830-B73-1deg	2017-08-30	03:12:06	J2253+1608	5.98	−0.690	44.0	45	2.90	3.8	4790
J2228-170830-B73-3deg	2017-08-30	04:00:44	J2253+1608	5.98	−0.690	48.9	45	2.51	4.6	4531
J0449-170830-B73-5deg[a]	2017-08-30	08:03:25	J0522−3627	4.44	−0.311	46.2	47	2.43	2.9	4783
J0449-170830-B73-7deg	2017-08-30	08:57:09	J0522−3627	4.44	−0.311	56.9	47	2.40	2.8	4799
J2228-170917-B73-1deg	2017-09-17	01:45:48	J2253+1608	5.41	−0.669	41.2	41	1.84	2.4	12115
J0633-170917-B73-1deg	2017-09-17	14:05:08	J0522−3627	4.04	−0.252	37.3	39	1.61	11.3	11373
J0633-170917-B73-4deg	2017-09-17	14:52:56	J0522−3627	4.04	−0.252	27.7	39	1.57	11.8	11366
J2228-170926-B73-1deg	2017-09-26	03:09:05	J2253+1608	4.94	−0.688	50.7	42	0.97	4.2	13916
J2228-170926-B73-3deg[b]	2017-09-26	03:47:41	J2253+1608	4.94	−0.688	49.3	42	1.05	5.2	13015
J2228-170926-B73-6deg	2017-09-26	04:38:23	J2253+1608	4.94	−0.688	44.4	42	1.04	5.2	11457
J0449-170928-B73-2deg	2017-09-28	09:02:33	J0522−3627	4.19	−0.179	75.8	43	0.52	4.9	14818
J0449-170929-B73-5deg	2017-09-29	07:05:54	J0522−3627	3.95	−0.179	58.2	42	1.27	7.5	14694
J0633-170930-B73-1deg[c d e]	2017- 09-30	09:41:19	J0522−3627	3.95	−0.179	75.6	48	0.83	3.6	14951
J0633-170930-B73-4deg[e f]	2017-09-30	08:51:18	J0522−3627	3.95	−0.179	75.6	48	0.83	3.6	14961
J0633-171001-B73-9deg[c]	2017-10-01	09:25:16	J0522−3627	3.95	−0.179	76.3	40	1.61	11.6	14470
Band 8-4										
J1709-170717-B84-2deg	2017-07-17	00:49:17	J1924−2914	2.68	−0.583	43.7	26	0.65	8.4	2058
J1709-170717-B84-1deg	2017-07-17	01:45:23	J1924−2914	2.68	−0.583	56.0	26	0.66	9.6	2058
J1709-170717-B84-11deg	2017-07-17	02:32:47	J1924−2914	2.68	−0.583	66.3	26	0.64	10.2	2055
J2228-170717-B84-7deg[c g]	2017-07-17	09:58:57	J2253+1608	4.98	−0.716	38.5	28	0.26	8.0	2249
J1259-170717-B84-1deg	2017-07-17	22:40:09	J1256−0547	6.72	−0.495	68.0	35	0.81	8.0	3447
J1259-170717-B84-8deg	2017-07-17	23:30:44	J1256−0547	6.72	−0.495	58.8	35	0.76	8.3	3327
J1259-170718-B84-11deg	2017-07-18	00:22:30	J1256−0547	6.72	−0.495	47.8	35	0.74	8.9	3229
J0633-170718-B84-1deg	2017-07-18	13:52:33	J0522−3627	5.11	−0.148	76.2	34	0.34	6.0	3649
J0633-170718-B84-4deg[h]	2017-07-18	14:41:55	J0522−3627	5.11	−0.148	74.6	34	0.41	5.7	3688
J0633-170718-B84-9deg	2017-07-18	16:48:00	J0522−3627	5.11	−0.148	52.7	34	0.59	5.6	3696
J0633-170718-B84-6deg	2017-07-18	15:55:11	J0522−3627	5.11	−0.148	63.0	34	0.52	5.6	3691
J2228-170819-B84-1deg[i]	2017-08-19	08:01:17	J2253+1608	5.34	−0.665	36.5	43	0.66	6.2	3290
J2228-170820-B84-3deg	2017-08-20	04:26:10	J2253+1608	4.62	−0.705	47.8	24	0.72	6.1	5016
J2228-170820-B84-10deg	2017-08-20	05:12:57	J2253+1608	4.62	−0.705	50.5	24	0.67	7.2	5322
J2228-170820-B84-1deg	2017-08-20	06:08:47	J2253+1608	4.62	−0.705	249.5	4	0.59	7.8	5357
Band 9-4										
J2228-170717-B94-1deg	2017-07-17	06:58:47	J2253+1608	3.37	−0.716	49.3	29	0.35	9.5	2343
Band 9-6										
J2228-170725-B96-1deg	2017-07-25	05:59:58	J2253+1608	3.26	−0.718	47.0	33	0.27	5.5	2943
J2228-170725-B96-6deg	2017-07-25	06:46:10	J2253+1608	3.26	−0.718	50.2	33	0.27	5.4	2851
J0449-170725-B96-5deg[c]	2017-07-25	11:06:01	J0522−3627	5.18	−0.184	54.3	22	0.43	5.0	2339
J0449-170725-B96-7deg[c]	2017-07-25	11:52:14	J0522−3627	5.18	−0.184	63.3	22	0.45	5.5	2340
J0449-170725-B96-12deg[c]	2017-07-25	13:41:00	J0522−3627	5.18	−0.184	76.6	26	0.45	5.3	2887
J2228-170825-B96-3deg	2017-08-25	04:35:49	J2253+1608	3.13	−0.705	49.9	46	0.41	4.7	4461
J2228-170828-B96-6deg[e]	2017-08-28	07:06:40	J2253+1608	3.13	−0.705	39.6	47	0.47	6.1	4792

Notes. The tests are ordered into band pairs, where the first band is that of the target and the following that of the calibrator for the B2B blocks only. Tests are identified by the target, the observing date (YYMMDD), the B2B frequency pair, and the related in-band calibrator separation angle in the naming scheme. Baseline length is the maximal projected value and are rounded to the nearest meter. The flux and spectral index (α) of the DGC source relate to the target observing frequency. The DGC source elevation, El., is given as that at the start of the observation. The wind speed is the average from all operational weather stations during the observing run.

[a] Five antennas flagged.
[b] Uses DGC block from J2228−170926-B73-1deg.
[c] Only has/uses one DGC block.
[d] Only has one in-band block.
[e] Six antennas flagged.
[f] All DGC blocks failed, used one from J0633−170930-B73-1deg.
[g] Only has one B2B block.
[h] One in-band block flagged as source >85° elevation.
[i] Last DGC block flagged.

high-frequency data after B2B phase calibration for the various cycle times. In this case, in Equation (4) $t = t_{\rm obs}$ and thus the entire postcalibration phase-time sequence is used. The result is the residual phase rms values for each cycle time $t_{\rm cyc}$ of 24, 48, 72, 96, and 120 s.

Table 2 lists the expected phase rms values (in degrees and microns) as a function of time averaged using only baselines longer than 1.5 km per observation. We average only these long baselines as we expect all baselines beyond this to have a similar phase rms value. This is a reasonable assumption when considering the maximal 129 s timescale over which we expect a frozen phase screen traveling at the maximal wind speed of our observations, $v_{\rm wind} = 11.8$ m s^{-1}, to have moved ($v_{\rm wind} t = 1520$ m). The listed phase rms in degrees is that calculated at the target high frequency via Equation (2).

3. Results

The following subsections address goal (3) outlined at the end of Section 1, first by considering the variation of phase rms with cycle time and the relationship to expected image coherence, and second by comparing the images of in-band and B2B techniques.

3.1. Phase rms Trends with Time

In Figure 2 we plot the expected phase rms values as measured from the DGC source over the timescales of 33, 81, and 129 s for all 44 data sets. The phase rms, in terms of microns of path length, spans from ∼20 to ∼700 μm for the lowest timescale and best stability, to the longest timescale and worst stability. Color represents the target frequency: blue is band 7, purple is band 8 and yellow is band 9, whereas the symbols are representative of the maximal baseline lengths: circles are for maximal baselines between 1.5 and 3.7 km, squares are for 3.7 to 8.5 km, while triangles are for baselines >8.5 km. Regardless of the absolute phase rms, spanning over an order of magnitude in scale, the power-law increase with time appears quite ubiquitous. The fit of the logarithm of the expected phase rms with time indicates powers ranging from 0.3 to 0.8, although the mean value is 0.52 ± 0.09, i.e., the expected phase rms, on average, scales with $\sqrt{\rm time}$ (the median slope is 0.5). We suggest that this slope is representative for observations within the range of our tests, e.g., where maximal baselines are >2000 m and for timescales up to ∼2 minutes. The bottom panel presents the zoom of observations with <100 μm expected phase rms (at t = 129 s).

For additional reference, the subaxis scales to the left and right provide an indication of the observing condition in terms of degrees of expected phase rms and expected coherence (using Equations (1) and (2)). Focusing on the lower panel, an expected phase rms <100 μm translates to <35° at band 7, and thus the expected coherence will be >0.8 provided phase calibration occurred with a cycle time, $t_{\rm cyc}$, less than 129 s. For the band 8 frequency used in these data (∼392-407 GHz) the expected coherence has a minimal value of ∼0.7, only slightly different from band 7. The expected coherence significantly drops, to below 0.4, at band 9 as the expected phase rms exceeds 80° for a 100 μm path length. Hence, if the post-phase-referencing (residual) phase rms of a given target is equivalent to the expected phase rms, then the image coherence would be equivalent to the estimated coherence. We explore this in Section 3.2 for the DGC source.

We also perform the same fitting on the residual phase rms of the DGC source, as noted above, this is measured from the high-frequency data after phase correction with various cycle times, 24, 48, 72, 96, and 120 s. A similar power-law trend is also clearly seen although the mean slope is slightly shallower at 0.39 ± 0.11 (median 0.38) but is still consistent with the aforementioned trend. In comparing the phase rms measures, expected (scaled to the relevant cycle times) and residual, we find that the 24 and 48 s residual phase rms values can be up to a factor of 2 larger than expected phase rms for some band 8 and 9 observation where the expected phase rms <20°. However, this difference for such low phase rms values means that the coherence measures are still within a 10%–15% agreement.

3.2. DGC Source Coherence Comparisons

In the top panel of Figure 3 we plot the expected coherence values against the measured image coherence of the DGC source. The dashed line is that of equality, whereas the dotted lines indicate ± 5% and 10% coherence difference moving farther from the line of equality, respectively. The expected coherence values are calculated using the expected phase rms measured on the DGC source over 33, 81, and 129 s, which are scaled to the nearest phase-referencing cycle time using $\sigma_\phi \propto \sqrt{\rm time}$, e.g., $\sigma_\phi(24\ {\rm s}) = \sigma_\phi(33)\sqrt{(24/33)}$. Recall that the expected phase rms in degrees as reported in Table 2 is relative to the high-frequency band. Thus, the scaled expected phase rms values should now be representative of those measured over a timescale equal to the cycle time. Likewise, the expected coherence should tie with the coherence of the image of the DGC source at the high frequency.

For all cycle times, the expected and measured image coherence are coincident, irrespective of maximal baseline length or frequency band, similar to results presented in Maud et al. (2020) (right panel of Figures 5 and 10), although in their work they did not make any time-scaling correction and hence compared images made with 24 s cycle times with the expected phase from the DGC over 33 s. The mean differences between expected and image coherence are <5% at band 7 for all cycle times; ∼5%, 8%, 12%, 11%, and 17% at band 8 for 24, 48, 72, 96, and 120 s cycle times respectively; and ∼5%, 6%, 9%, 10%, and 15% at band 9, again for 24, 48, 72, 96, and 120 s cycle times, respectively. Note that the images where the expected and measured image coherence differ by more than 50% were excluded in the statistics, these being data typically taken in unsuitable conditions and consequently having <0.5 image coherence in general.

In the bottom panel of Figure 3 the residual phase rms is instead used to calculate the expected coherence, i.e., the phase fluctuations that actually remain in the DGC source data at the high-frequency band after phase calibration using B2B. As above, in comparing the expected and image coherence values, while excluding those different by more than 50%,we find the mean differences are <6% for all band 7 cycle times; ∼2%, 5%, 9%, 14%, and 11% at band 8; and ∼2%, 6%, 6%, 7%, and 13% at band 9, for 24, 48, 72, 96, and 120 s cycle times, respectively. All values of the expected and image coherence are provided in Table 3.

Table 2
Average Expected Phase rms as Measured from the DGC Source over ∼33, 81, and 129 s Using Baselines >1500 m

Name	Microns			Degrees		
	33 s	81 s	129 s	33 s	81 s	129 s
Band 7-3						
J2228-170827-B73-1deg	35.4	56.8	70.3	11.9	19.0	23.5
J2228-170829-B73-1deg	42.0	60.1	73.6	14.1	20.1	24.7
J2228-170829-B73-3deg	55.5	81.0	96.3	18.6	27.1	32.3
J2228-170829-B73-6deg	41.6	62.4	77.5	13.9	20.9	26.0
J0449-170829-B73-2deg	38.8	59.7	76.0	13.0	20.0	25.5
J0449-170829-B73-3deg	42.2	69.2	89.7	14.1	23.2	30.1
J2228-170830-B73-1deg	50.0	80.1	96.4	16.7	26.8	32.3
J2228-170830-B73-3deg	45.8	82.5	114.0	15.3	27.6	38.2
J0449-170830-B73-5deg	45.2	78.3	97.2	15.2	26.2	32.6
J0449-170830-B73-7deg	33.6	51.3	65.6	11.2	17.2	22.0
J2228-170917-B73-1deg	59.7	90.5	109.0	20.0	30.3	36.5
J0633-170917-B73-1deg	153.8	248.4	300.6	51.5	83.2	100.7
J0633-170917-B73-4deg	270.0	483.1	621.3	90.4	161.9	208.2
J2228-170926-B73-1deg	30.2	49.9	60.5	10.1	16.7	20.3
J2228-170926-B73-3deg	36.5	60.5	77.0	12.2	20.3	25.8
J2228-170926-B73-6deg	35.2	55.1	70.5	11.8	18.4	23.6
J0449-170928-B73-2deg	51.0	81.3	95.6	17.1	27.2	32.0
J0449-170929-B73-5deg	88.8	135.3	163.0	29.7	45.3	54.6
J0633-170930-B73-1deg	22.2	35.2	43.5	7.4	11.8	14.6
J0633-170930-B73-4deg[a]	22.2	35.3	43.5	7.4	11.8	14.6
J0633-171001-B73-9deg	239.8	391.8	486.0	80.3	131.3	162.8
Band 8-4						
J1709-170717-B84-2deg	72.1	107.6	130.8	34.1	50.9	61.9
J1709-170717-B84-1deg	57.2	102.5	117.9	27.0	48.5	55.8
J1709-170717-B84-11deg	69.0	126.1	155.6	32.6	59.7	73.6
J2228-170717-B84-7deg	105.8	188.5	208.1	50.0	89.2	98.5
J1259-170717-B84-1deg	52.5	87.8	114.8	24.8	41.6	54.3
J1259-170717-B84-8deg	48.3	80.1	105.2	22.8	37.9	49.8
J1259-170718-B84-11deg	61.6	100.3	113.1	29.2	47.4	53.5
J0633-170718-B84-1deg	35.8	61.5	75.3	16.9	29.1	35.6
J0633-170718-B84-4deg	30.7	46.1	54.3	14.5	21.8	25.7
J0633-170718-B84-9deg	46.6	71.9	87.4	22.1	34.0	41.4
J0633-170718-B84-6deg	51.7	82.8	98.7	24.5	39.2	46.7
J2228-170819-B84-1deg	39.8	67.5	84.2	18.8	31.9	39.8
J2228- 170820-B84-3deg	107.8	171.2	212.8	51.0	81.0	100.7
J2228-170820-B84-10deg	90.5	171.2	230.9	42.8	81.0	109.2
J2228-170820-B84-1deg	88.8	166.4	222.5	42.0	78.7	105.3
Band 9-4						
J2228-170717-B94-1deg	40.6	55.7	62.8	33.2	45.5	51.3
Band 9-6						
J2228-170725-B96-1deg	19.3	29.0	34.2	15.8	23.8	28.0
J2228-170725-B96-6deg	16.1	29.3	41.4	13.2	24.0	33.9
J0449-170725-B96-5deg	17.2	33.5	47.6	14.1	27.4	39.0
J0449-170725-B96-7deg	28.7	50.0	65.1	23.5	41.0	53.3
J0449-170725-B96-12deg	18.9	28.3	32.0	15.4	23.2	26.2
J2228-170825-B96-3deg	34.0	49.8	57.5	27.8	40.8	47.2
J2228-170828-B96-6deg	35.4	65.6	85.0	28.9	53.8	69.7

Notes. Uncertainties in the phase rms estimates of 20% are not unreasonable.
[a] Uses phase rms values from J0633-170930-B73-1deg.

Overall, for images with coherence values >0.8 the expected and image coherence are within 5%. Therefore, if the phase rms for a given timescale is <40°, then the predicted coherence will be an excellent proxy for the real image coherence if phase referencing was made using a cycle time equal to that timescale. With a broad-brush approach, it could be assumed that the expected and image coherence values are within 5%–10% for shorter cycle times (<72 s) and within 10%–15% for longer cycle times (>72 s), irrespective of the observing band or maximum baseline length investigated here. Critically,

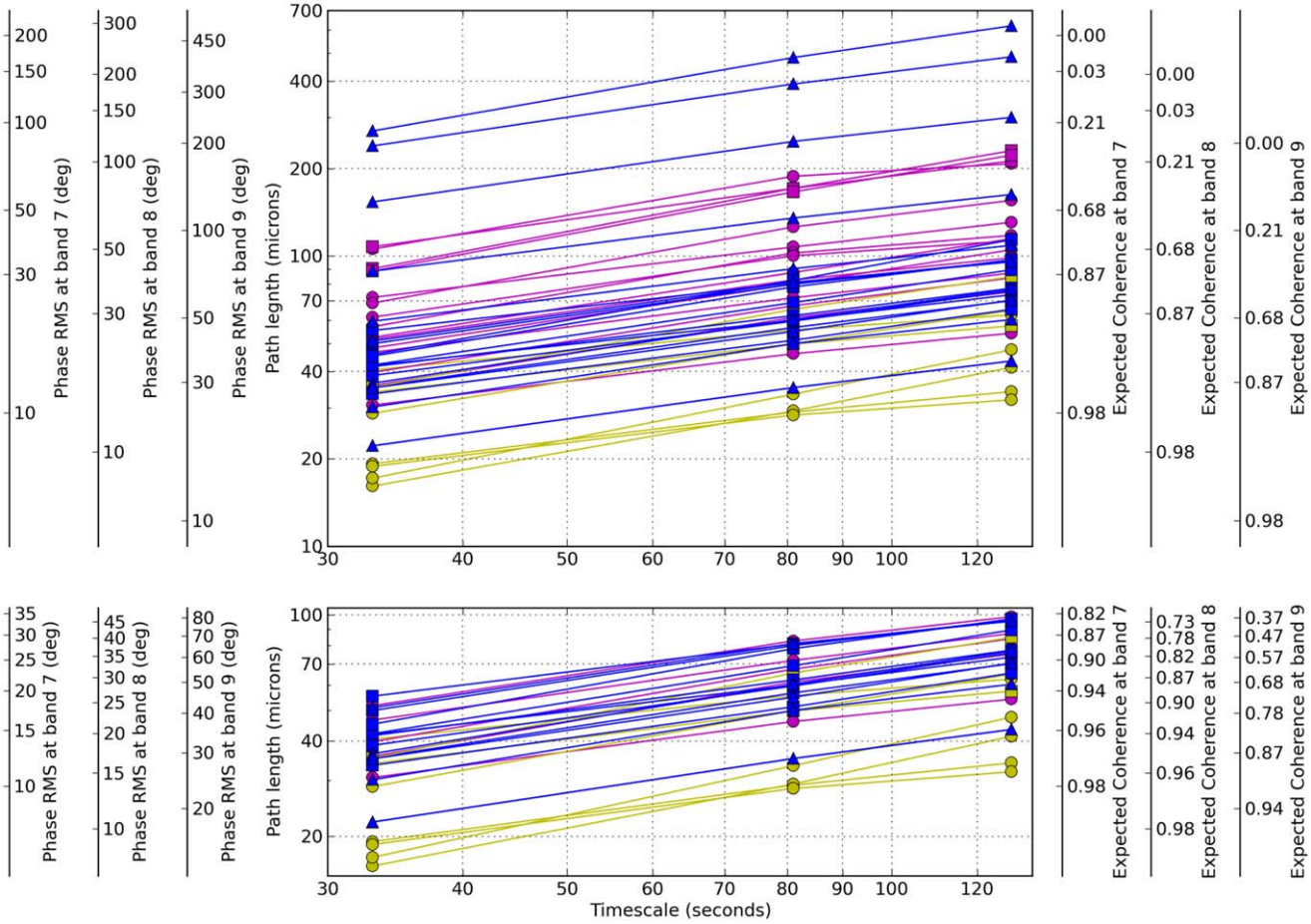

Figure 2. Expected phase rms presented in path-length microns against the measurement timescale. The left scale bars show the phase rms at bands 7, 8, and 9 in degrees, while the right scale bars show the expected coherence. The bottom panel presents a zoom in of data with a maximal expected phase rms of 100 μm. The color relates to the target frequency: blue is band 7, purple is band 8, and yellow is band 9. The symbols are representative of the maximal baseline lengths: circles are for maximal baselines between 1.5 km and 3.7 km, squares are for 3.7 km to 8.5 km, while triangles are for baselines >8.5 km. Independent of the absolute phase rms value, maximal baseline length of the data, or the frequency bands, the phase rms all increase as a power law, following an average of $\sim\sqrt{\text{time}}$.

however, one must remember that these DGC source images use phase referencing of the same source in B2B mode, i.e., where there is no angular separation angle difference.

3.3. Target Image Coherence with Cycle Time

In 16 data sets, the in-band and B2B blocks have the same phase calibrator, all of which are within 2° of the target. The frequency pairings B7-3 (9), B8-4 (5), B9-4 (1), and B9-6 (1) are covered. The remaining 28 observations pairing B7-3 (12), B8-4 (10), and B9-6 (6) have phase calibrators for the in-band block ranging from ∼2° to ∼11° separation from the target, whereas the paired B2B blocks used a close calibrator within 1.°67. The underlying reason to use different calibrators was to mimic the use case of the B2B technique (see Maud et al. 2020).

3.3.1. In-band and B2B Close Calibrators

Figure 4 shows the coherence values taken from the in-band and B2B images (left and right) as a function of cycle time, from observations using the same, close, phase calibrator. Both in-band and B2B calibrated data show a decreasing trend with increasing cycle time. Such curves are expected to follow an exponential decrease because the image and expected coherence are well correlated, and the expected coherence is simply derived from the expected phase rms via a negative exponential in Equation (1). For our high-coherence data (>0.8) the trends could be assumed to be linear, and only those with a lower coherence (<0.6) show a somewhat exponential-like decline.

Figure 4 quite clearly visualizes that high-coherence data sets, $\simeq 0.9$ for the 24 s cycle time, degrade very little with increasing cycle time. These are data with low (good) expected phase rms ($\sigma_\phi < 20°$–$25°$). For over a factor of 4 increase in time, the coherence drops by around 0.1. On the contrary, when the image coherence is already <0.6 at 24 s cycle times, corresponding to data with high expected phase rms (poor stability, $\sigma_\phi > 50°$–$60°$), the coherence drops by a further 0.3 when increasing the cycle time to 120 s. The black dashed lines show the theoretical expected coherence calculated from the phase rms, where the upper and lower lines have $\sigma_\phi = 30°$ and 90° at 120 s, respectively, using the phase rms $\propto \sqrt{\text{time}}$ relationship. The image improvement with cycle time follows this general trend but does not show exactly the same coherence improvement as theorized, moving from longer to short cycle times. This is likely due to a combination of the finite calibrator separation angle, as the target and phase calibrator do have different lines of sight through the atmosphere although they are close (<1.°67), and the fact that the phase rms as a function of time deviates from the $\sqrt{\text{time}}$ average trend. The in-band and B2B image coherence values are given in Table 4 for all close calibrator observations.

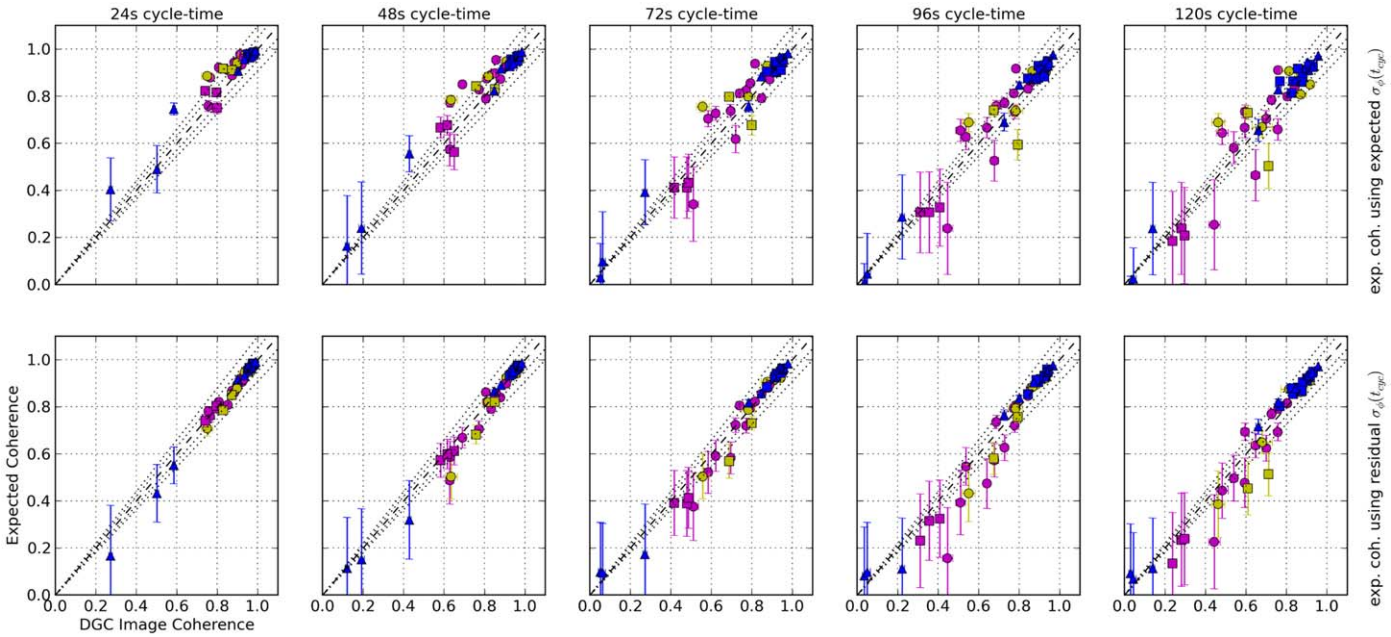

Figure 3. Comparisons of the DGC source image coherence after calibration using 24, 48, 72, 96, and 120 s cycle times, compared with the expected coherence. The top panel calculates the expected coherence using the expected phase rms measured on the DGC over 33, 81, and 129 s timescales after scaling to the respective cycle time of the calibrated data. The bottom panel instead uses the residual phase rms, the variations measured to remain in the DGC high-frequency data after B2B phase referencing. The colors (bands) and symbols (baseline length) follow those in Figure 2. The dashed line is that of equality, whereas the dotted lines are differences of ± 5% and ± 10% respectively. Essentially, the expected coherence calculated using either the expected or residual phase rms is in strong agreement with the image coherence for all cycle times.

For these observations with close calibrators, if the phase rms is already good for the chosen cycle time (e.g., $\sigma_\phi < 30°$–$40°$ for 120 s cycle times) then the act of fast switching does not significantly improve the image coherence. The value of using fast cycle times in this case is diminishing. Critically, however, for observations in poor stability, $\sigma_\phi > 70°$($t_{cyc} = 120$ s), fast switching can recover these into usable data ($\sigma_\phi < 50°$, coherence > 0.65–0.70), while for marginal stability conditions with $\sigma_\phi \sim 50°$–$70°$($t_{cyc} = 120$ s), the mediocre-quality images can be transformed into good ones ($\sigma_\phi < 30°$–$40°$, coherence > 0.75–0.80). This is highlighted in Figure 5, which shows images of the target source J2228-0753, calibrated using J2229-0832 separated by only $0\overset{\circ}{.}68$, with cycle times of 24, 72, and 120 s (top to bottom) in stable conditions on 2017 August 19 (left) and unstable conditions on 2017 August 20 (right). In stable conditions, the coherence and dynamic range of the target degrade very little even when considering the factor of 5 longer cycle time from top to bottom. The point-source image structure also remains unchanged. On the contrary, in unstable conditions, the fastest cycle time provides a considerably better image, remaining point like at $\sim 3\sigma$ and achieving $>60\%$ coherence. For the longer cycle times, the coherence plummets, and in the worst case, the dynamic range is a factor of 2 worse. The longer cycle time images also show defects with an equivalent size scale to that of the beam at levels $>5\sigma$. If this were a more complex science source, such defects would impact the scientific interpretation.

3.3.2. In-band Distant, and B2B Close Calibrators

Considering the data sets with different phase calibrators, where in-band used more distant ones while B2B still used close ones, the trends of image coherence with cycle time are clearly different between in-band and B2B. Figure 6 divides bands 7, 8, and 9 into the top, middle, and bottom panels for clarity. The bands 7 and 8 B2B observations in the top and middle right-hand panels show the same results as Figure 4, because B2B used similarly close phase calibrators. The left, top, and middle panels for in-band observations however show a major difference in the trend with cycle time. Irrespective of the expected phase rms, there are little to no changes in the measured image coherence with cycle time for any of the observations, independent of the maximum baseline lengths. The image coherence is decoupled from the expected phase rms. Using distant calibrators does not aid in correcting the phase fluctuations to the level expected regardless of the cycle time and furthermore could also include the negative effects of unmeasured and unmodeled differences in zenith path delay between distant antennas or the so-called antenna position uncertainties (see also Asaki et al. 2020b; Hunter et al. 2016; Maud et al. 2020). Previous work by Asaki et al. (2016) also indicated that the postcalibration phase rms is not reduced by phase referencing using distant calibrators compared to the precalibration phase rms, even when using fast switching.

The trends in the band 9 data sets appear slightly different. This, however, is a side effect of not being able to self-calibrate the weak targets and our use of the estimated fluxes for the targets in calculating the image coherence. All band 9 observations were conducted in stable conditions ($\sigma_\phi < 30°$ over 33 s), and so the coherence is expected to be >0.85 and consequently not expected to degrade much with increasing cycle time. Using assumed band 9 fluxes for the targets means the image coherence suffers from a large uncertainty (± 20%). For the B2B observations (bottom-right panel), the coherence upper limit is consistent with the bands 7 and 8 B2B data, in that images with coherence values >0.7–0.8 do not degrade

Table 3
Expected and Image Coherence Values for the DGC Source as a Function of Cycle Time

Name	Expected (Using Expected $\sigma_\phi(t_{cyc})$)					Expected (Using Residual $\sigma_\phi(t_{cyc})$)					Image (t_{cyc})				
	24 s	48 s	72 s	96 s	120 s	24 s	48 s	72 s	96 s	120 s	24 s	48 s	72 s	96 s	120 s
Band 7-3															
J2228-170827-B73-1deg	0.98	0.97	0.95	0.94	0.92	0.98	0.98	0.96	0.96	0.95	0.98	0.96	0.95	0.94	0.93
J2228-170829-B73-1deg	0.98	0.96	0.95	0.93	0.92	0.95	0.94	0.93	0.91	0.88	0.95	0.93	0.91	0.89	0.86
J2228-170829-B73-3deg	0.96	0.93	0.91	0.88	0.86	0.96	0.93	0.88	0.85	0.80	0.96	0.92	0.87	0.84	0.77
J2228-170829-B73-6deg	0.98	0.96	0.94	0.92	0.91	0.98	0.97	0.95	0.93	0.92	0.97	0.96	0.95	0.93	0.90
J0449-170829-B73-2deg	0.98	0.96	0.95	0.93	0.91	0.98	0.96	0.95	0.93	0.91	0.98	0.96	0.94	0.93	0.90
J0449-170829-B73-3deg	0.98	0.96	0.93	0.91	0.88	0.98	0.96	0.94	0.92	0.91	0.98	0.95	0.92	0.91	0.88
J2228-170830-B73-1deg	0.97	0.94	0.91	0.88	0.86	0.96	0.94	0.93	0.91	0.85	0.96	0.94	0.92	0.90	0.83
J2228-170830-B73-3deg	0.97	0.95	0.90	0.87	0.81	0.97	0.96	0.93	0.91	0.88	0.97	0.95	0.92	0.88	0.83
J0449-170830-B73-5deg	0.97	0.95	0.91	0.88	0.86	0.98	0.97	0.94	0.93	0.87	0.98	0.96	0.94	0.92	0.88
J0449-170830-B73-7deg	0.99	0.97	0.96	0.95	0.93	0.98	0.97	0.96	0.95	0.93	0.98	0.97	0.95	0.94	0.92
J2228-170917-B73-1deg	0.96	0.92	0.88	0.85	0.83	0.93	0.89	0.86	0.84	0.82	0.93	0.88	0.85	0.80	0.76
J0633-170917-B73-1deg	0.75	0.56	0.39	0.29	0.24	0.55	0.32	0.17	0.11	0.11	0.59	0.43	0.27	0.22	0.14
J0633-170917-B73-4deg	0.40	0.16	0.03	0.01	0.00	0.17	0.11	0.10	0.08	0.09	0.27	0.12	0.05	0.04	0.03
J2228-170926-B73-1deg	0.99	0.98	0.96	0.95	0.94	0.98	0.97	0.96	0.95	0.93	0.98	0.97	0.95	0.93	0.90
J2228-170926-B73-3deg	0.98	0.97	0.95	0.93	0.91	0.98	0.97	0.96	0.95	0.93	0.98	0.97	0.95	0.94	0.91
J2228-170926-B73-6deg	0.98	0.97	0.95	0.94	0.92	0.98	0.98	0.96	0.96	0.94	0.98	0.97	0.96	0.95	0.93
J0449-170928-B73-2deg	0.97	0.94	0.90	0.87	0.86	0.97	0.95	0.92	0.90	0.88	0.97	0.94	0.91	0.87	0.84
J0449-170929-B73-5deg	0.91	0.82	0.76	0.69	0.66	0.92	0.87	0.82	0.76	0.72	0.90	0.85	0.78	0.73	0.66
J0633-170930-B73-1deg	0.99	0.99	0.98	0.98	0.97	0.99	0.99	0.98	0.97	0.97	0.99	0.98	0.98	0.97	0.96
J0633-170930-B73-4deg[a]	0.99	0.99	0.98	0.98	0.97	0.99	0.99	0.98	0.97	0.97	0.99	0.98	0.98	0.97	0.96
J0633-171001-B73-9deg	0.49	0.24	0.10	0.04	0.02	0.43	0.15	0.09	0.10	0.07	0.50	0.19	0.06	0.05	0.04
Band 8-4															
J1709-170717-B84-2deg	0.88	0.77	0.70	0.63	0.58	0.76	0.59	0.52	0.55	0.50	0.76	0.63	0.58	0.54	0.54
J1709-170717-B84-1deg	0.92	0.85	0.73	0.65	0.64	0.82	0.67	0.59	0.39	0.44	0.81	0.69	0.62	0.51	0.48
J1709-170717-B84-11deg	0.89	0.79	0.62	0.53	0.46	0.87	0.86	0.72	0.57	0.64	0.87	0.81	0.72	0.68	0.65
J2228-170717-B84-7deg	0.76	0.57	0.34	0.24	0.25	0.78	0.49	0.38	0.16	0.23	0.76	0.63	0.51	0.45	0.44
J1259-170717-B84-1deg	0.93	0.87	0.79	0.73	0.66	0.91	0.84	0.85	0.72	0.69	0.92	0.88	0.85	0.78	0.76
J1259-170717-B84-8deg	0.94	0.89	0.82	0.77	0.70	0.86	0.79	0.72	0.63	0.62	0.88	0.83	0.77	0.73	0.70
J1259-170718-B84-11deg	0.91	0.83	0.74	0.67	0.67	0.81	0.71	0.58	0.47	0.48	0.85	0.77	0.70	0.64	0.59
J0633-170718-B84-1deg	0.97	0.94	0.89	0.86	0.84	0.94	0.91	0.88	0.88	0.86	0.94	0.91	0.88	0.86	0.84
J0633-170718-B84-4deg	0.98	0.95	0.94	0.92	0.91	0.92	0.86	0.82	0.81	0.79	0.91	0.86	0.82	0.78	0.76
J0633-170718-B84-9deg	0.95	0.90	0.86	0.81	0.78	0.89	0.84	0.79	0.79	0.77	0.90	0.85	0.79	0.77	0.73
J0633-170718-B84-6deg	0.94	0.88	0.81	0.76	0.73	0.89	0.82	0.81	0.73	0.69	0.90	0.81	0.74	0.69	0.60
J2228-170819-B84-1deg	0.96	0.92	0.87	0.83	0.80	0.91	0.90	0.89	0.85	0.81	0.93	0.91	0.89	0.84	0.80
J2228-170820-B84-3deg	0.75	0.56	0.41	0.31	0.24	0.79	0.61	0.39	0.32	0.23	0.80	0.65	0.48	0.36	0.28
J2228-170820-B84-10deg	0.82	0.67	0.41	0.31	0.18	0.80	0.57	0.39	0.23	0.13	0.80	0.58	0.42	0.31	0.24
J2228-170820-B84-1deg	0.82	0.68	0.43	0.33	0.21	0.74	0.60	0.41	0.32	0.24	0.74	0.62	0.49	0.41	0.30
Band 9-4															
J2228-170717-B94-1deg	0.89	0.78	0.76	0.69	0.69	0.71	0.50	0.50	0.43	0.39	0.75	0.63	0.56	0.55	0.46
Band 9-6															
J2228-170725-B96-1deg	0.97	0.95	0.93	0.90	0.89	0.94	0.92	0.91	0.91	0.88	0.93	0.92	0.91	0.89	0.87
J2228-170725-B96-6deg	0.98	0.96	0.92	0.90	0.85	0.95	0.94	0.92	0.92	0.91	0.96	0.96	0.94	0.93	0.92
J0449-170725-B96-5deg	0.98	0.96	0.90	0.87	0.81	0.94	0.94	0.91	0.89	0.86	0.94	0.93	0.91	0.88	0.87
J0449-170725-B96-7deg	0.94	0.88	0.80	0.74	0.67	0.88	0.82	0.79	0.79	0.65	0.90	0.82	0.78	0.78	0.68
J0449-170725-B96-12deg	0.97	0.95	0.93	0.91	0.91	0.95	0.93	0.91	0.88	0.87	0.94	0.91	0.88	0.87	0.81
J2228- 170825-B96-3deg	0.92	0.84	0.80	0.74	0.73	0.79	0.68	0.57	0.58	0.45	0.83	0.76	0.69	0.67	0.61
J2228-170828-B96-6deg	0.91	0.83	0.68	0.59	0.50	0.85	0.82	0.73	0.76	0.51	0.87	0.85	0.8	0.79	0.71

Notes. The expected coherence using the expected phase rms from Table 2 is scaled to the cycle time following $\sqrt{\text{time}}$ and shown in the leftmost columns. The expected coherence using the residual phase rms is in the central columns. Independent of the phase rms used, the expected coherence is calculated using Equation (1).
[a] Uses phase rms values from J0633-170930-B73-1deg.

significantly with cycle time when using close phase calibrators. Conversely, we see that the in-band image coherence values (bottom-left panel) are considerably lower than the paired B2B ones, even when considering an upper limit. Thus, the fact that the in-band, band 9 observations have a low and constant image coherence again points to a decoupling from the expected phase rms and where the large calibrator to target separation angle limits the phase correction effectiveness. In comparing only image peak fluxes the in-band images are lower than the B2B counterpart images. The

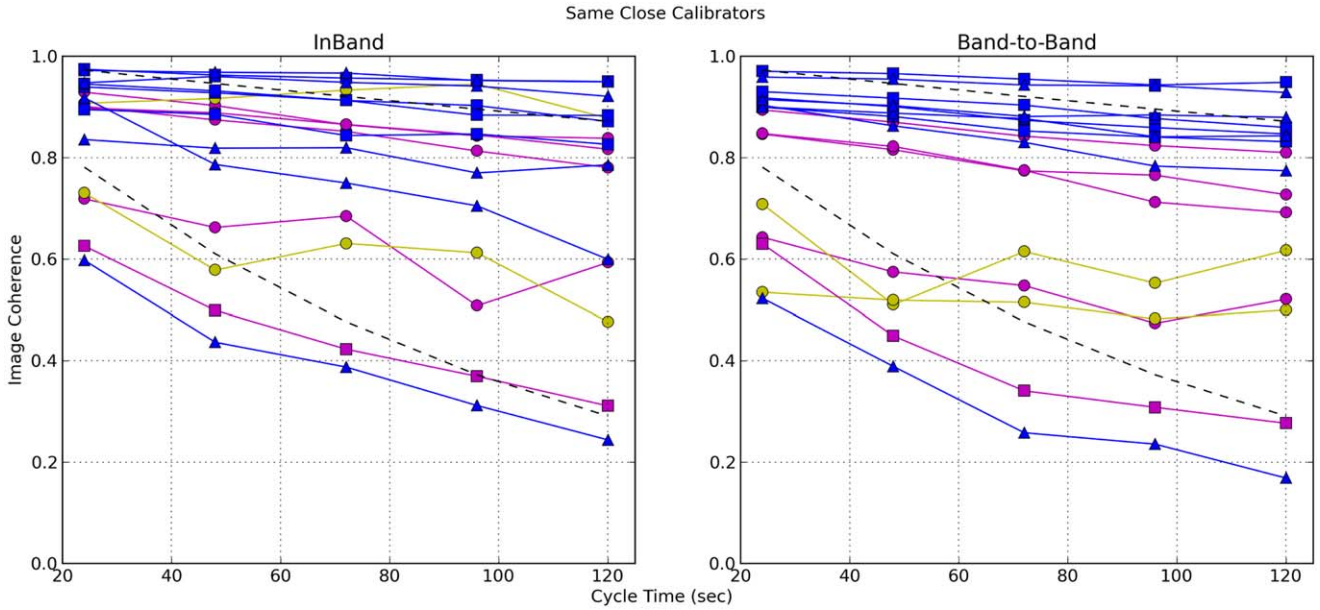

Figure 4. Image coherence as a function of phase-referencing cycle time (24, 48, 72, 96, 120 s) at bands 7, 8, and 9, for both in-band (left) and B2B (right) images that are calibrated with the same close $<1\overset{\circ}{.}67$ calibrators. The colors (bands) and symbols (baseline length) follow those in Figure 2. For all observations, regardless of frequency or maximal baseline length, there is a clear decrease of coherence as a function of time. The black dashed line indicates theoretical expected coherence values, where the upper and lower lines are related to $\sigma_\phi = 30^\circ$ and 90° at the 120 s cycle time and assume a $\sqrt{\text{time}}$ scaling to shorter times. Faster switching provides a significant improvement for low coherence, where the phase rms can be improved from a poor to reasonable value. There is little change for observations with already good phase rms (high coherence). Uncertainties are not included for plotting clarity but are of the order $\pm 5\%$ for bands 7 and 8, and typically $\pm 20\%$ for band 9.

Table 4
In-band and B2B Image Coherence Values for All Cycle Times from Observations Using Close Calibrators

Name	In-band					B2B				
	24 s	48 s	72 s	96 s	120 s	24 s	48 s	72 s	96 s	120 s
Band 7-3										
J2228-170827-B73-1deg	0.97	0.96	0.96	0.95	0.95	0.97	0.97	0.96	0.94	0.95
J2228-170829-B73-1deg	0.94	0.93	0.91	0.90	0.87	0.92	0.90	0.87	0.86	0.85
J0449-170829-B73-2deg	0.90	0.89	0.84	0.85	0.83	0.90	0.88	0.85	0.84	0.83
J2228-170830-B73-1deg	0.95	0.93	0.91	0.88	0.88	0.93	0.92	0.90	0.88	0.86
J2228-170917-B73-1deg	0.92	0.79	0.75	0.71	0.60	0.90	0.86	0.83	0.78	0.77
J0633-170917-B73-1deg	0.60	0.44	0.39	0.31	0.24	0.52	0.39	0.26	0.24	0.17
J2228-170926-B73-1deg	0.95	0.96	0.95	0.94	0.92	0.96	0.96	0.94	0.94	0.93
J0449-170928-B73-2deg	0.84	0.82	0.82	0.77	0.79	0.90	0.89	0.88	0.84	0.84
J0633-170930-B73-1deg	0.97	0.97	0.97	0.95	0.95	0.92	0.90	0.88	0.88	0.88
Band 8-4										
J1709-170717-B84-1deg[a]	0.72	0.66	0.69	0.51	0.59	0.64	0.57	0.55	0.47	0.52
J1259-170717-B84-1deg	0.90	0.87	0.85	0.81	0.78	0.85	0.82	0.77	0.77	0.73
J0633-170718-B84-1deg	0.93	0.90	0.87	0.84	0.84	0.89	0.87	0.84	0.82	0.81
J2228-170819-B84-1deg[a]	0.90	0.89	0.87	0.84	0.82	0.85	0.82	0.78	0.71	0.69
J2228-170820-B84-1deg[a]	0.63	0.50	0.42	0.37	0.31	0.63	0.45	0.34	0.31	0.28
Band 9-4										
J2228-170717-B94-1deg[b]	0.73	0.58	0.63	0.61	0.48	0.71	0.51	0.62	0.55	0.62
Band 9-6										
J2228-170725-B96-1deg[b]	0.91	0.92	0.93	0.95	0.88	0.53	0.52	0.52	0.48	0.50

Notes.
[a] Indicates that the image coherence was calculated against the self-calibrated image that used a solution interval of the scan duration (∼9 s).
[b] Indicates that the image coherence was calculated against the expected band 9 flux after extrapolation from self-calibrated band 7 and band 8 images.

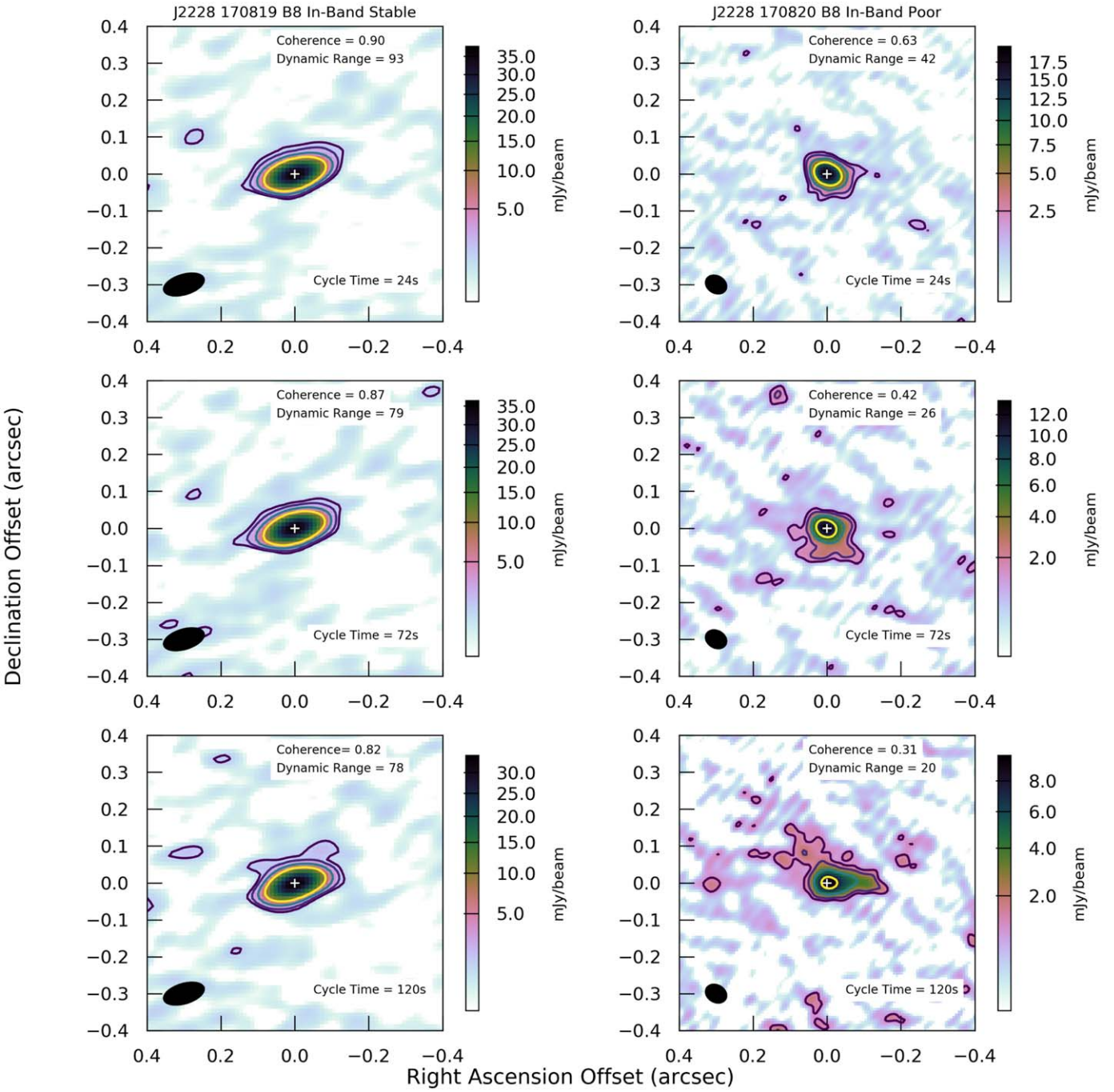

Figure 5. Images of the target source J2228-0753 at band 8 using normal in-band phase referencing and calibrated with J2229-0832, separated by only 0.°68. From top to bottom are the images calibrated with 24, 72, and 120 s cycle times, while left and right can be considered stable and unstable conditions taken on 2017 August 19 and 20, respectively. The expected phase rms values using Table 2 and scaling by $\sqrt{\text{time}}$ are 15.°3, 30.°1, and 38.°4 and 43.°5, 76.°4, and 97.°1 at 24, 72, and 120 s cycle times for the stable and unstable conditions, respectively. The images are all scaled to their respective peak flux densities while the contours are at 1.2, 2.0, 4.0, and 8.0 mJy bm^{-1} and correspond approximately to 2σ–3σ, 4σ–5σ, 9σ–10σ, and 18σ–20σ.

in-band and B2B image coherence values for observations with distant in-band calibrators are listed in Table 5.

In general, for all bands, the in-band image coherence values are lower than expected and fall below those of the corresponding B2B paired observation. This is better seen in Figure 7, which compares the in-band and B2B observations of the 16 data sets with the same calibrators in the top panels and the 28 data sets where in-band used distant calibrators in the bottom ones. In the top panel, the in-band and B2B values are almost equivalent when the same phase calibrator is used, as previously reported by Maud et al. (2020) provided that the small detrimental effects of DGC for the B2B mode are acknowledged (<5%–10% coherence losses). In the bottom panel we clearly see that at short cycle times the B2B images with close calibrators are vastly superior, while only for longer cycle times do the B2B image coherence values become more similar to the in-band ones. This emphasizes that distant phase calibrators have the same effect as imposing a long phase-referencing cycle time. We discuss the phase error budget further in Section 4.2.

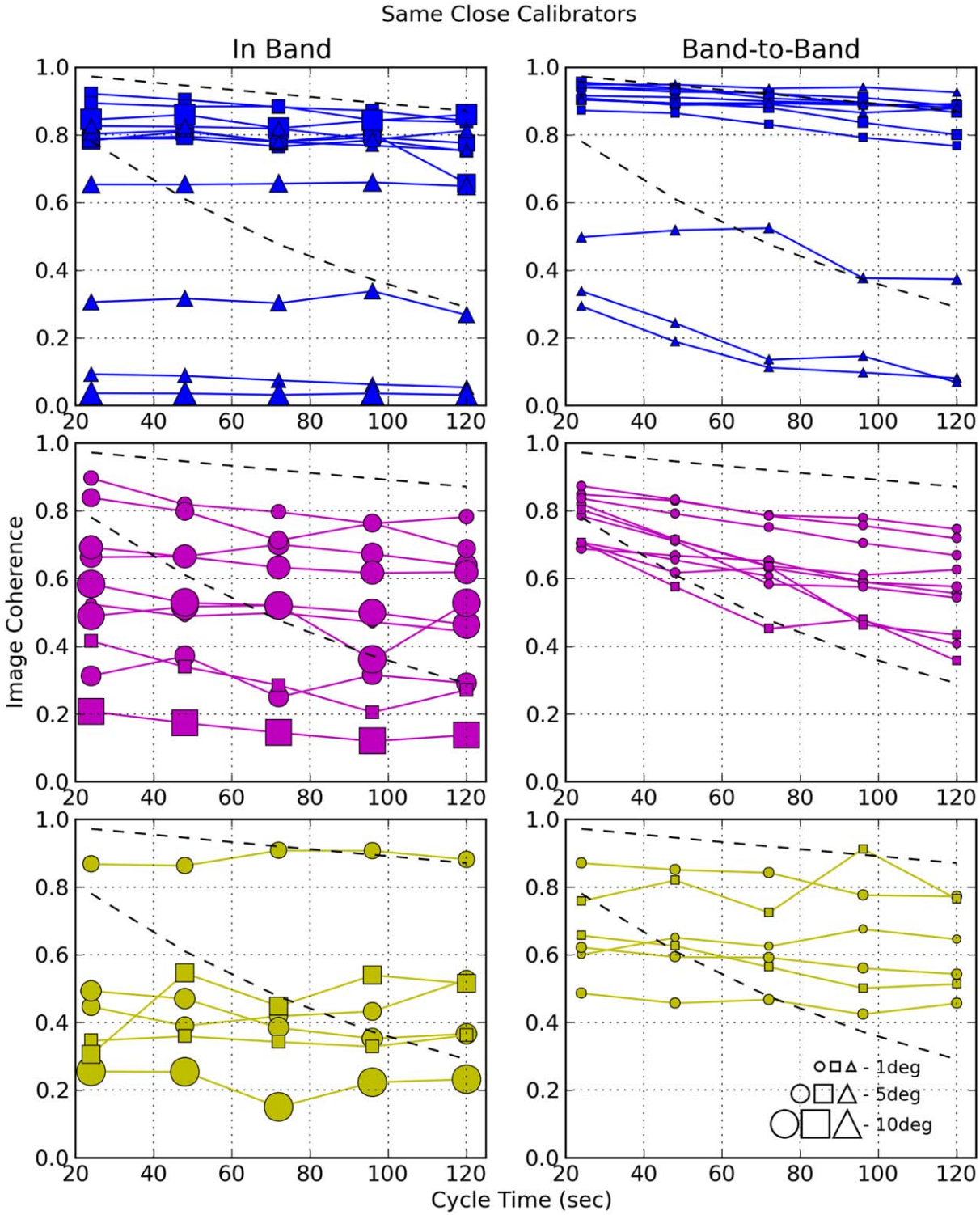

Figure 6. Image coherence as a function of phase-referencing cycle time (24, 48, 72, 96, 120 s) at bands 7, 8, and 9 (top to bottom), for both in-band (left) and B2B (right) images. The in-band observations used more distant calibrators (between ∼2° and 11°) whereas the B2B images, like those in Figure 4, use close calibrators (<1.°67). The colors (bands) and symbols (baseline length) follow those in Figure 2 except that the symbol size now indicates the calibrator separation angle as shown in the legend in the bottom-right panel. The upper and lower black lines are related to $\sigma_\phi = 30°$ and 90° at the 120 s cycle time and assume a $\sqrt{\text{time}}$ scaling to shorter times. The left panel shows that for distant calibrators the coherence changes very little with cycle time. The right panel shows no difference from Figure 4 where coherence follows the expected reduction with increasing cycle time. Note that although all band 9 observations were taken in stable conditions, the targets could not be self-calibrated, and estimated fluxes were used in the calculation of coherence, leading to large uncertainties and likely underestimates (see the text). Comparing left and right panels, the coherence values are always lower for in-band distant calibrators versus the respective B2B calibration using a close calibrator. Uncertainties are not included for plotting clarity but are of the order ± 5% for bands 7 and 8, and typically ± 20% for band 9.

Table 5
In-band and B2B Image Coherence Values for All Cycle Times Where In-band Observations Used Distant Calibrators Compared to B2B Observations Using Close Calibrators

Name	In-band					B2B				
	24 s	48 s	72 s	96 s	120 s	24 s	48 s	72 s	96 s	120 s
Band 7-3										
J2228-170829-B73-3deg	0.79	0.79	0.77	0.79	0.75	0.87	0.86	0.83	0.79	0.77
J2228-170829-B73-6deg	0.78	0.81	0.78	0.80	0.66	0.92	0.91	0.90	0.89	0.88
J0449-170829-B73-3deg	0.92	0.90	0.88	0.87	0.84	0.96	0.94	0.91	0.90	0.87
J2228-170830-B73-3deg	0.89	0.88	0.89	0.84	0.84	0.94	0.93	0.92	0.89	0.89
J0449-170830-B73-5deg	0.79	0.80	0.78	0.79	0.78	0.90	0.89	0.88	0.84	0.80
J0449-170830-B73-7deg	0.85	0.86	0.82	0.84	0.86	0.94	0.93	0.92	0.91	0.89
J0633-170917-B73-4deg	0.09	0.09	0.07	0.06	0.05	0.29	0.19	0.11	0.10	0.08
J2228-170926-B73-3deg	0.80	0.81	0.78	0.77	0.75	0.91	0.89	0.89	0.87	0.88
J2228-170926-B73-6deg	0.65	0.65	0.66	0.66	0.65	0.95	0.95	0.94	0.94	0.93
J0449-170929-B73-5deg	0.31	0.32	0.30	0.34	0.27	0.50	0.52	0.52	0.38	0.37
J0633-170930-B73-4deg	0.83	0.82	0.82	0.79	0.81	0.9	0.89	0.89	0.89	0.88
J0633-171001-B73-9deg	0.04	0.04	0.03	0.04	0.03	0.34	0.24	0.14	0.15	0.07
Band 8-4										
J1709-170717-B84-2deg[a]	0.62	0.57	0.59	0.55	0.52	0.80	0.71	0.72	0.67	0.64
J1709-170717-B84-11deg[a]	0.49	0.52	0.52	0.50	0.46	0.69	0.67	0.65	0.59	0.58
J2228-170717-B84-7deg[a]	0.31	0.37	0.25	0.32	0.29	0.71	0.65	0.61	0.48	0.41
J1259-170717-B84-8deg	0.66	0.67	0.70	0.67	0.64	0.82	0.72	0.64	0.61	0.63
J1259-170718-B84-11deg	0.58	0.53	0.52	0.36	0.53	0.79	0.71	0.58	0.58	0.54
J0633-170718-B84-4deg	0.90	0.82	0.80	0.76	0.78	0.85	0.83	0.79	0.78	0.75
J0633-170718-B84-9deg	0.69	0.66	0.63	0.62	0.62	0.84	0.79	0.75	0.71	0.67
J0633-170718-B84-6deg	0.84	0.80	0.71	0.76	0.69	0.87	0.83	0.79	0.76	0.72
J2228-170820-B84-3deg[a]	0.42	0.34	0.29	0.21	0.27	0.71	0.58	0.45	0.48	0.36
J2228- 170820-B84-10deg[a]	0.21	0.17	0.15	0.12	0.14	0.8	0.72	0.64	0.46	0.44
Band 9-6										
J2228-170725-B96-6deg[b]	0.53	0.46	0.49	0.51	0.62	0.71	0.77	0.74	0.80	0.76
J0449-170725-B96-5deg[b]	0.91	0.91	0.95	0.95	0.93	0.51	0.48	0.49	0.45	0.48
J0449-170725-B96-7deg[b]	0.52	0.49	0.40	0.37	0.38	0.91	0.89	0.88	0.81	0.81
J0449-170725-B96-12deg[b]	0.27	0.27	0.16	0.23	0.24	0.65	0.62	0.62	0.59	0.57
J2228-170825-B96-3deg[b]	0.41	0.42	0.41	0.39	0.43	0.78	0.74	0.67	0.59	0.61
J2228-170828-B96-6deg[b] [c]	...	...	...	...	...	0.90	0.97	0.86	1.08	0.90

Notes.
[a] Indicates that the image coherence was calculated against the self-calibrated image that used a solution interval of the scan duration (∼9 s).
[b] Indicates that the image coherence was calculated against the expected band 9 flux after extrapolation from self-calibrated band 7 and band 8 images.
[c] The target could not be images with in-band calibration. The B2B 96 s cycle time coherence values exceeds 1.0, indicating that the reference-expected self-calibrated source flux was underestimated.

4. Analysis and Discussion

In this section we investigate the effective baseline-length parameterizations and the phase error budget for our observations. The effective baseline length can be an important parameter to know as observers may be able to use it to understand and estimate the expected array performance. We test how good (i) the theoretical parameterization using the effective baseline length, which incorporates the calibrator separation angle and cycle time, and (ii) a phase stability measurement (estimated phase rms) combined with the empirical trend of image coherence degradation as a function of calibrator separation angle are for estimating the final target image coherence in phase-referencing scenarios. We also propose a pragmatic approach to optimizing future ALMA observations with dynamic cycle times and calibrator integration times.

4.1. Inspecting the Effective Baseline Length

In principle the phase rms at the effective baseline length, $B_{\rm eff,calc}$ (see also Section 1) should be the value that all other longer baselines should achieve after phase referencing for a given cycle time. As highlighted in Carilli & Holdaway (1999), applying phase referencing on short timescales using fast switching achieves small $B_{\rm eff,calc}$ theoretically, thus facilitating observations and imaging using arbitrarily long-baseline arrays. Prior to observing, if one has access to an SSF plot, from a stare observation of a strong point source or from a phase-monitor system, then in theory it would be possible to use a fitting method to obtain $B_{\rm eff,fit}$ and thus find the phase rms and subsequently use it to decide whether the observation should take place or not (under the caveat that the monitoring direction and elevation were close to those of the target of interest). The VLA employs a two-element atmospheric-seeing monitor to

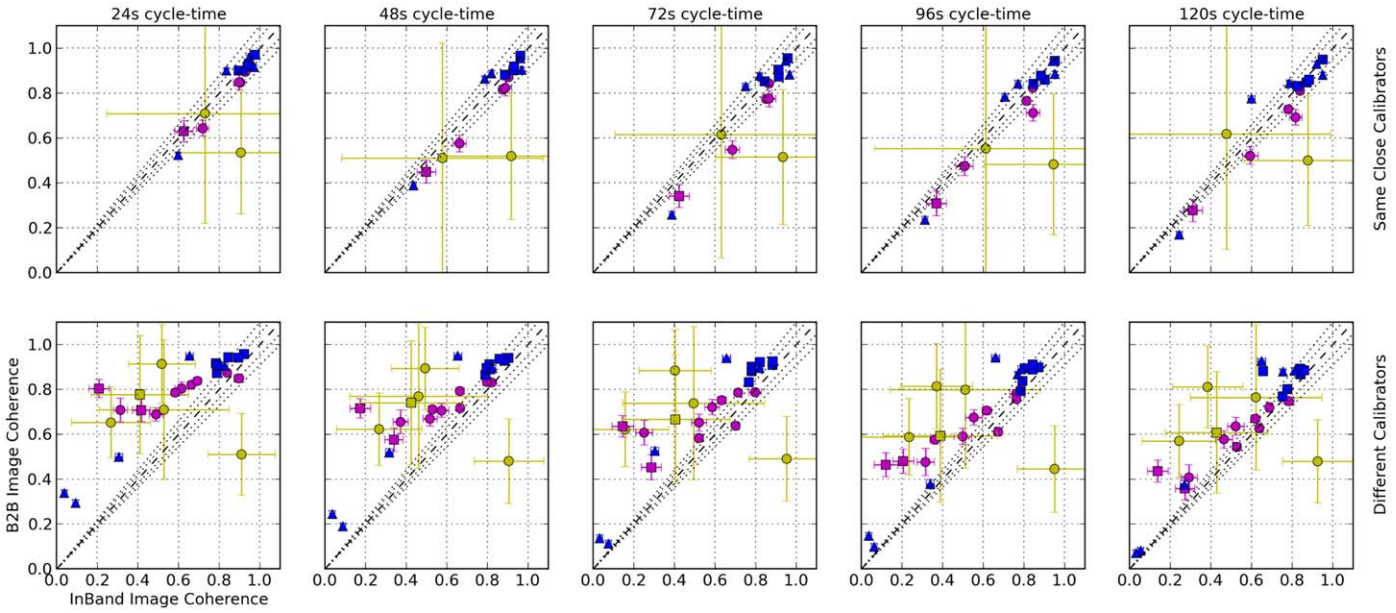

Figure 7. Image coherence comparing in-band and B2B images for various cycle times (24, 48, 72, 96, 120 s). The upper panels show the 16 data sets where in-band and B2B used the same close calibrator, while the bottom show the 28 data sets where in-band use distant calibrators. As previously shown in Maud et al. (2020) when using close calibrators, in-band and B2B are have almost coincident image coherence values. When in-band calibrators are more distant, the B2B images are far superior, especially for short cycle times, where the phase rms due to atmospheric fluctuation can be minimized using close calibrators. These in-band images have effectively constant image coherence values regardless of cycle time and are only most coincident with B2B observations for the longest cycle time, where the phase rms of the B2B data with close calibrators worsens. This supports that using distant calibrators, regardless of cycle time, is the same as using close calibrators with long cycle times—the phase error budgets become similar (see Section 4.2). The colors (bands) and symbols (baseline length) follow those in Figure 2 while errors are propagated from an uncertainty in the peak flux density of three times the image noise level.

aid scheduling (Morris 2014). Holdaway & Owen (1995) present an updated expression of the expected phase rms after phase correction related to the effective baseline length (see Holdaway 1992), which is $B_{\rm eff,calc} = v_{\rm wind} t_{\rm cyc}/2$ for phase referencing with a zero degree separated source (i.e., the DGC sources for our observations are self-referenced using B2B transfer). This result was derived from their VLA data using the SSF of a target quasar before and after calibration and simulations.

4.1.1. Establishing Effective Baseline Length Measures

Here we want to consider if the aforementioned theoretical parameterization from Holdaway & Owen (1995) is suitable for ALMA. We are aware that the ALMA site topography is different to that of the VLA and as such we follow a data-driven approach and resample the data from Holdaway & Owen (1995) in order to derive an appropriate methodology for ALMA. Figure 8 shows the SSF of the source 2131−021 resampled from Figure 1 in Holdaway & Owen (1995). The black crosses mark the uncalibrated data, the classical SSF, whereas the blue squares indicate the calibrated data where solutions were provided from a nearby source, 2134+004, with an 80 s cycle time. This could be assumed as a time-sampled SSF for $t = 80$ s (e.g., Equation (4)). The key point is to find the baseline length where the phase rms from the uncalibrated data SSF is matched with the residual phase rms of the calibrated data, which is seen to be constant for longer baselines. Holdaway & Owen (1995) reported that $B_{\rm eff,fit} \sim 400$ m and hence defined $B_{\rm eff,calc} = v_{\rm wind} t_{\rm cyc}/2 + d$, where they assumed the target–calibrator separation d provided a negligible contribution (see also Section 4.2) and for a typical wind speed of $\sim$10 m s^{-1}. In deriving our methodology we explicitly separate the nomenclature of the theoretically calculated effective baseline length using observing parameters, $B_{\rm eff,calc}$, from the fitted effective baseline, $B_{\rm eff,fit}$, as measured from the data. $B_{\rm eff,fit}$ is the baseline length where the expected phase rms calculated using baselines >1500 m intersects with a linear fit to the uncalibrated data SSF. We assume baselines >1500 m are longer than $B_{\rm eff,calc}$ and thus within a regime where the phase rms should be constant; see also Section 2.2 and Figure 8 blue square symbols). In Figure 8 the black dashed line indicates the linear fit (log–log) to the uncalibrated SSF which has a slope of 0.44 ± 0.01, i.e., $b^{0.44}$ (the dotted lines shows the range of the gradient), while the solid horizontal purple line shows the average phase rms of the calibrated data measured from baseline >1500 m. The dashed purple line indicates the extrapolation to shorter baseline until reaching the intersection point with the line fitted to the uncalibrated data SSF at $B_{\rm eff,fit}$. Thus, the fitted effective baseline length is $B_{\rm eff,fit} = 412\ ^{+69}_{-57}$ m and is represented by the star symbol in Figure 8. Our fitted value is consistent with the theoretical effective baseline length, $B_{\rm eff,calc} \sim 400$ m and corroborates our fitting methodology.

4.1.2. Extending the Methodology to the ALMA Data

We find that fits are possible for all data sets, although we exclude J2228-170717-B84-7deg because for longer cycle times there are phase unwrapping issues and a number of baselines have an abnormally high-phase rms. The fitted effective baseline lengths are listed in Table 6. Typically, the $B_{\rm eff,fit}$ values are significantly less than the longest baselines in the array and highlights the advantage of such fast switching in being able to correct the phase rms down to a very low level (with the caveat that these data are from the DGC source and phase referencing does not change sky position). An example

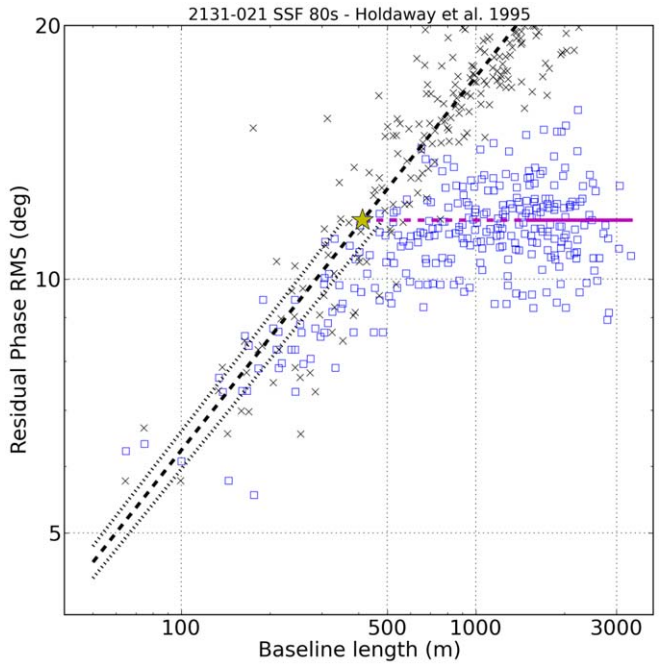

Figure 8. SSF plot extracted from Figure 1 of Holdaway & Owen (1995) for the source 2131−021. The uncalibrated data are shown by black crosses, whereas the calibrated data, using solutions from a nearby source 2134+004 and an 80 s cycle time, are shown as blue squares. These data were originally used to indicate that the phase rms saturated after the effective baseline, $B_{\rm eff,calc} = v_{\rm wind} t_{\rm cyc}/2 \sim 400$ m, when comparing the uncalibrated SSF with the mean phase rms after calibration ($\sim$12°), and considering a the typical site wind speed of $\sim$10 m s^{-1}. Our fitting method suggests that $B_{\rm eff,fit}$ 412^{+69}_{-57} m, as indicated by the star symbol. The black dashed line is the linear regression to the uncalibrated SSF in log–log space, while the dotted lines indicate the error ranges in the gradient. The solid purple line represents the mean phase rms measured for baselines >1500 m, while the dashed purple line is the continuation to shorter baselines until the intercept with the slope of the uncalibrated SSF.

case of a reasonably well-fit observation is shown in Figure 9, where the black crosses represent the uncalibrated SSF, and the blue squares represent the expected phase rms. The star symbol identifies the location of $B_{\rm eff,fit}$, which can clearly be seen to increase with increasing cycle time, indicative of the worsening phase rms. In establishing $B_{\rm eff,fit}$ we use the DGC expected phase rms data from 33, 81, and 129 s timescales rescaled to the cycle times (24, 48, 72, 96, 120 s) in order to calculate the mean expected phase rms values, which are then compared with the fit to the uncalibrated DGC source SSFs. In fitting the uncalibrated SSF we select only baselines between 100 and 700 m as Matsushita et al. (2017) indicated that ALMA SSFs often have a breakpoint around 1000 m. A handful of our observations tentatively have uncalibrated data SSFs without a distinct turnover or only show a slight shallowing, which Matsushita et al. (2017) suggest could be due to conditions in which the height of the turbulent constituents are >1000 m.

4.1.3. Comparing the Fitted and Theoretical Values of Effective Baseline Length

In Figure 10 we present the ratio of $B_{\rm eff,fit}/B_{\rm eff,calc}$ as a function of cycle time, wind speed, and time of day referenced to midnight (Chilean Local Time, CLT = UTC−4 h). In the left panel we offset (in time) the different frequency bands for plotting clarity, whereas the middle and right panels show the mean ratio considering all timescales (uncertainties being the standard deviation). In general, there is little change of the ratio as a function of cycle time. This is not unexpected. Phase rms follows $\sim b^{0.6}$ (Matsushita et al. 2017) for baselines <1000 m and is also proportional to $\sqrt{\rm time}$ (Section 3.1), such that the relationship between time and effective baseline length is almost constant. The three horizontal lines indicate an equal ratio and those a factor of two discrepant. The majority of analyzed observations, 23 of 43, fall between ratios of one and two. Otherwise, there are 12 and 8 observations with ratios <1 and >2, respectively.

The middle panel of Figure 10 clearly indicates the association of high-ratio data sets as those with low wind speeds <4–5 m s^{-1}. Tentatively there does appear to be a trend between $B_{\rm eff,fit}/B_{\rm eff,calc}$ and wind speed for these low wind speed observations, although only 5 of the 44 total data sets have a ratio >2.5. Such large ratios already point to either the measured ground wind speeds being an inadequate representation of the tropospheric phase screen speed, or where the frozen screen approximation itself breaks down. The mean ratio values for all data sets with wind speeds >4, >5 and >6 m s^{-1} are 1.29 ± 0.56, 1.24 ± 0.56 and 1.16 ± 0.51 respectively. These average ratios are in reasonable agreement with theory when accounting for a proposed wind speed scaling factor of 1.2 suggested by Ishizaki & Sakamoto (2005). This factor would act to correct the wind speed as measured on the weather mast at the ALMA site to that of the aloft tropospheric turbulent phase screen, $v_{\rm screen} = 1.2 \times v_{\rm wind}$, where $v_{\rm screen}$ should be the value which is used in the calculation of $B_{\rm eff,calc}$.

In the right panel of Figure 10 we see some tentative separation of ratios related to the observing time. Following Ishizaki & Sakamoto (2005) we separate into day and night using times of 0900–1800 and 1800–0900 CLT, respectively. There are 7 daytime observations, 6 of these have a $B_{\rm eff,fit}/B_{\rm eff,calc}$ ratio <1 and none have low wind speeds. The average ratio from these observations is 0.83 ± 0.69, which reduces to 0.57 ± 0.24 excluding the one observation with a >2 ratio. These low ratios are contrary to the above overall mean ratios (all observations), pointing to the fact that those were dominated by the 36 nighttime observations. Of the nighttime observation there are 23 with $B_{\rm eff,fit}/B_{\rm eff,calc}$ between 1 and 2, with an average of 1.54 ± 0.28, 6 with a ratio <1, while the remaining 7 have a ratio >2. Of these high ratio nighttime observations all but one have ratios >2.5 and are the low wind-speed data sets. When excluding the low wind speed observations, the average ratio for nighttime observations is 1.40 ± 0.46. Even when considering the uncertainties and the low number statistics for the day time observations we find that day and night observations appear to represent distinctly low and high $B_{\rm eff,fit}/B_{\rm eff,calc}$ ratios respectively. The ratios are presented in Table 7.

The low ratios of $B_{\rm eff,fit}/B_{\rm eff,calc}$ occurring during the daytime point to the theoretical parameterization overestimating $B_{\rm eff,calc}$ and would lead to higher phase rms estimates than the data would really have. Holdaway et al. (2004) suggest that for fast switching ($t_{\rm cyc}$ ~20–30 s), most of the target integrations will be closer in time to the calibrator scans than $t_{\rm cyc}/2$, such that the phase discrepancy will be less than that measured at exactly the integration time of $t_{\rm cyc}/2$. These authors report that $v_{\rm wind} t_{\rm cyc}/2$ is an overestimate and should be further corrected when compared with their previous work (see Holdaway 1992; Holdaway & Owen 1995). Dependent on which corrections they account for in their simulations,

Table 6
Fitted Effective Baseline Length ($B_{\rm eff,fit}$) Using the SSF for the DGC Source

Name	Cycle Time				
	24 s	48 s	72 s	96 s	120 s
Band 7-3					
J2228-170827-B73-1deg[a]	97^{+23}_{-17}	194^{+54}_{-39}	353^{+111}_{-78}	445^{+147}_{-102}	544^{+186}_{-128}
J2228-170829-B73-1deg	41^{+6}_{-5}	101^{+20}_{-16}	135^{+29}_{-22}	196^{+46}_{-35}	243^{+59}_{-44}
J2228-170829-B73-3deg	93^{+18}_{-14}	170^{+38}_{-29}	214^{+50}_{-38}	274^{+68}_{-51}	$301^{+75}_{-56.0}$
J2228-170829-B73-6deg	87^{+22}_{-16}	193^{+58}_{-41}	278^{+90}_{-63}	387^{+134}_{-91}	481^{+173}_{-118}
J0449-170829-B73-2deg	91^{+22}_{-16}	215^{+62}_{-45}	339^{+108}_{-75}	483^{+164}_{-113}	650^{+233}_{-159}
J0449-170829-B73-3deg	121^{+28}_{-21}	233^{+63}_{-46}	373^{+110}_{-79}	489^{+152}_{-108}	635^{+206}_{-145}
J2228-170830-B73-1deg	110^{+21}_{-17}	232^{+52}_{-40}	376^{+93}_{-70}	512^{+133}_{-99}	587^{+157}_{-116}
J2228-170830-B73-3deg	88^{+20}_{-15}	166^{+43}_{-32}	312^{+92}_{-66}	407^{+127}_{-90}	591^{+197}_{-137}
J0449-170830-B73-5deg	171^{+46}_{-33}	335^{+102}_{-73}	602^{+206}_{-142}	796^{+286}_{-195}	$956.0^{+355.0}_{-240}$
J0449-170830-B73-7deg	123^{+30}_{-22}	275^{+79}_{-57}	417^{+129}_{-91}	583^{+192}_{-134}	777^{+269}_{-186}
J2228-170917-B73-1deg	219^{+110}_{-65}	386^{+219}_{-125}	510^{+307}_{-171}	646^{+407}_{-223}	$717.0^{+462.0}_{-251}$
J0633-170917-B73-1deg	69^{+25}_{-16}	119^{+50}_{-31}	172^{+80}_{-48}	215^{+105}_{-63}	240^{+120}_{-72}
J0633-170917-B73-4deg	78^{+60}_{-29}	128^{+114}_{-51}	206^{+209}_{-88}	253^{+270}_{-111}	305^{+340}_{-136}
J2228-170926-B73-1deg	39^{+32}_{-14}	110^{+126}_{-48}	237^{+338}_{-115}	363^{+582}_{-187}	448^{+759}_{-236}
J2228-170926-B73-3deg	70^{+104}_{-33}	186^{+383}_{-101}	385^{+990}_{-227}	578^{+1670}_{-355}	$810^{+2579}_{-513.0}$
J2228-170926-B73-6deg	112^{+131}_{-49}	236^{+343}_{-116}	365^{+596}_{-189}	498^{+881}_{-267}	$654^{+1241}_{-360.0}$
J0449-170928-B73-2deg	132^{+165}_{-60}	281^{+436}_{-142}	454^{+801}_{-242}	622^{+1189}_{-343}	681^{+1330}_{-379}
J0449-170929-B73-5deg	78^{+115}_{-37}	183^{+358}_{-98}	282^{+630}_{-159}	403^{+999}_{-236}	473^{+1229}_{-282}
J0633-170930-B73-1deg	129^{+175}_{-61}	246^{+405}_{-126}	368^{+676}_{-198}	481^{+950}_{-266}	569^{+1175}_{-320}
J0633-170930-B73-4deg[b]	128^{+179}_{-61}	245^{+415}_{-127}	366^{+696}_{-199}	480^{+980}_{-268}	$568^{+1214.0}_{-323}$
J0633- 171001-B73-9deg	288^{+425}_{-143}	482^{+815}_{-254}	695^{+1286}_{-381}	861^{+1679}_{-481}	990^{+1998}_{-561}
Band 8-4					
J1709-170717-B84-2deg	129^{+29}_{-22}	262^{+70}_{-51}	358^{+101}_{-73}	480^{+143}_{-103}	559^{+172}_{-122}
J1709-170717-B84-1deg	73^{+17}_{-13}	138^{+38}_{-28}	259^{+83}_{-58}	338^{+114}_{-78}	349^{+119}_{-82}
J1709-170717-B84-11deg	170^{+45}_{-33}	345^{+106}_{-75}	714^{+251}_{-172}	957^{+355}_{-240}	1148^{+438}_{-294}
J2228-170717-B84-7deg[c]	376^{+187}_{-112}	740^{+421}_{-242}	1417^{+907}_{-500}	1877^{+1261}_{-683}	1799^{+1200}_{-651}
J1259-170717-B84-1deg	133^{+50}_{-33}	297^{+134}_{-83}	556^{+284}_{-170}	776^{+423}_{-248}	1091^{+632}_{-363}
J1259-170717-B84-8deg	82^{+16}_{-13}	165^{+39}_{-29}	279^{+73}_{-54}	373^{+104}_{-76}	507^{+150}_{-108}
J1259-170718-B84-11deg	80^{+20}_{-15}	164^{+49}_{-35}	227^{+73}_{-51}	288^{+98}_{-67}	279^{+94}_{-65}
J0633-170718-B84-1deg	38^{+13}_{-8}	114^{+53}_{-32}	151^{+76}_{-45}	220^{+120}_{-69}	220^{+121}_{-69}
J0633-170718-B84-4deg	6^{+1}_{-1}	19^{+7}_{-4}	33^{+14}_{-9}	54^{+28}_{-16}	62^{+34}_{-19}
J0633-170718-B84-9deg	39^{+16}_{-10}	103^{+55}_{-31}	175^{+107}_{-58}	262^{+178}_{-93}	324^{+230}_{-118}
J0633-170718-B84-6deg	28^{+16}_{-8}	91^{+78}_{-35}	193^{+204}_{-83}	313^{+376}_{-145}	377^{+473}_{-178}
J2228-170819-B84-1deg	85^{+18}_{-14}	175^{+44}_{-33}	315^{+90}_{-65}	426^{+129}_{-92}	526^{+165}_{-117}
J2228-170820-B84-3deg	158^{+112}_{-56}	281^{+228}_{-109}	402^{+354}_{-164}	510^{+474}_{-214}	598^{+575}_{-255}
J2228-170820-B84-10deg	162^{+84}_{-49}	268^{+156}_{-87}	475^{+312}_{-167}	586^{+401}_{-212}	759^{+548}_{-283}
J2228-170820-B84-1deg	134^{+83}_{-44}	227^{+161}_{-82}	407^{+331}_{-159}	507^{+432}_{-204}	656^{+591}_{-272}
Band 9-4					
J2228-170717-B94-1deg	56^{+18}_{-12}	124^{+50}_{-32}	146^{+61}_{-39}	202^{+91}_{-56}	201^{+91}_{-56}
Band 9-6					
J2228-170725-B96-1deg	104^{+38}_{-25}	200^{+85}_{-54}	273^{+124}_{-77}	358^{+173}_{-105}	387^{+190}_{-115}
J2228-170725-B96-6deg	90^{+43}_{-26}	162^{+91}_{-51}	294^{+188}_{-101}	375^{+254}_{-134}	549^{+403}_{-206}
J0449-170725-B96-5deg	89^{+95}_{-38}	142^{+176}_{-65}	252^{+367}_{-124}	306^{+471}_{-154}	419^{+701}_{-219}
J0449-170725-B96-7deg	38^{+30}_{-14}	110^{+127}_{-48}	284^{+431}_{-142}	444^{+757}_{-234}	692^{+1321}_{-382}
J0449-170725-B96-12deg	183^{+199}_{-80}	343^{+439}_{-163}	459^{+631}_{-225}	595^{+873}_{-301}	596^{+874}_{-301}
J2228-170825-B96-3deg	55^{+15}_{-11}	136^{+47}_{-32}	194^{+73}_{-48}	283^{+116}_{-75}	300^{+125}_{-80}
J2228-170828-B96-6deg	89^{+45}_{-26}	205^{+128}_{-69}	501^{+384}_{-191}	708^{+583}_{-282}	988^{+868}_{-408}

Notes.
[a] Mean phase rms recalculated using baselines between 1000 and 1200 m to exclude a noisy baseline group.
[b] Uses last DGC block from J0633−170930-B73-1deg.
[c] Problematic high-phase rms baselines skewing fitting and mean values.

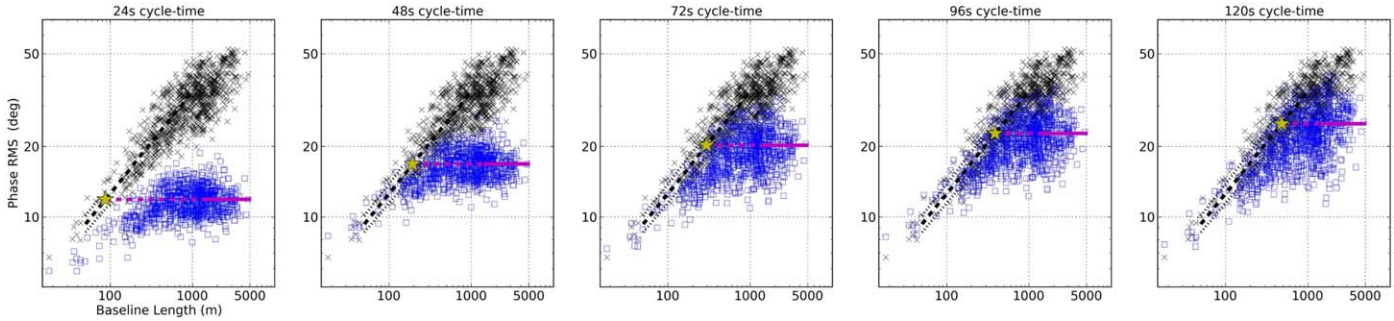

Figure 9. SSF plots from the DGC source as part of data set J2228-170829-B73-6deg before and after calibration. The five panels left to right show data calibrated with cycle times of 24, 48, 72, 96, and 120 s. The uncalibrated SSF is extracted from the DGC source phases with long-term slopes removed and are shown as black cross symbols. This is unchanged in each panel. The expected phase rms use the values measured on the DGC source at 33 s scaled to 24 and 48 s cycle times, 81 s scaled to 72 and 96 s cycle times, and 129 s scaled to the 120 s cycle time and are shown as blue squares. For shorter to longer cycle times it is clear to see the increasing expected phase rms. The star symbol indicates $B_{\rm eff,fit}$, which also increases with cycle time. The lines are as described in the text and the caption of Figure 8.

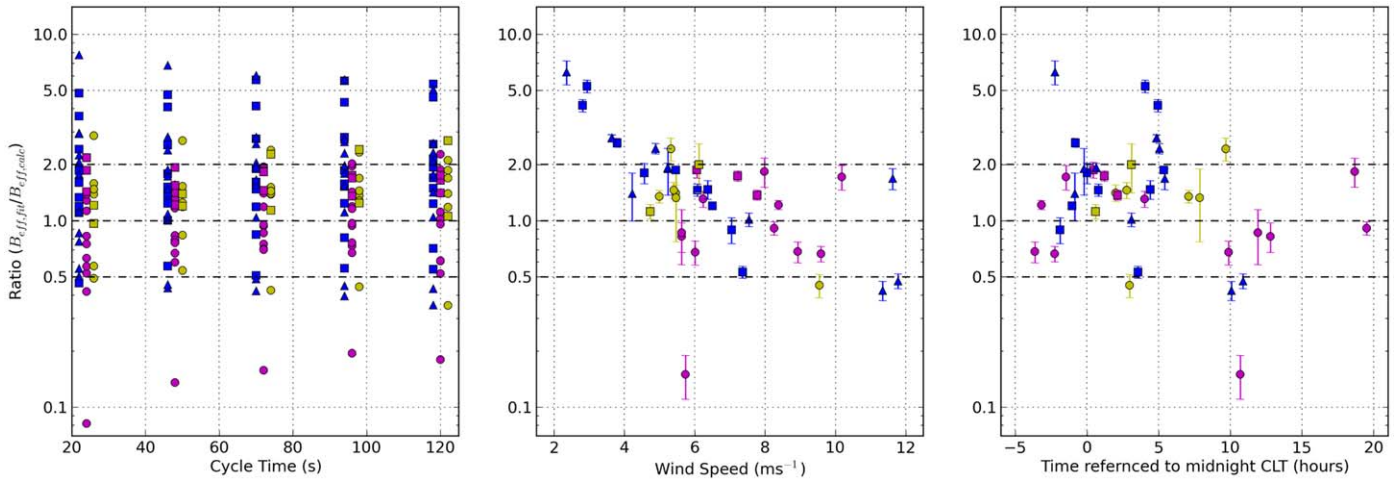

Figure 10. Plot of $B_{\rm eff,fit}/B_{\rm eff,calc}$ as a function of cycle time, wind speed, and observing time referenced to Chilean local midnight (CLT=UTC—4 h), in the left, middle and right panels respectively. Error bars are not included in the left panel but can account for a ratio change of ∼0.5 given the spread in $B_{\rm eff,fit}$. Typically there is little change in ratio with cycle time and the majority of observations fall within a ratio between one and two. The plot in the middle panel clearly indicates that low wind speed data sets do not match the theoretical prediction and that $B_{\rm eff,fit}$ is always higher than predicted. These data sets have a much larger phase rms than estimated. Tentatively there is a trend of decreasing ratio with wind speed, although only 5 of 44 data sets have a ratio >2.5. The right panel indicates some separation of predominantly low and high ratio observations into day (0900–1800) and night (1800–0900) time respectively. The uncertainties plotted in the middle and right panels are the standard deviation from averaging the five cycle time values. The colors (bands) and symbols (baseline length) follow those in Figure 2.

Holdaway et al. (2004) suggest that the phase rms could differ by between 0.65 and 0.93. This means that the effective baseline length should be scaled down by ratios of 0.49 and 0.89, respectively, compared with $B_{\rm eff,calc} = v_{\rm wind} t_{\rm cyc}/2$, and therefore points to our low-ratio daytime observations agreeing with the updated simulations and theory in Holdaway et al. (2004), i.e., a turbulent atmospheric screen advecting the array. We do caution however that this is based only on six of our data sets. We also propose that the actual scaling may be related not only to $t_{\rm cyc}$, but more so to the lengths of the target and phase calibrator scans, and the ratio between them. However, such an investigation is beyond the scope of this paper.

Scaling down the effective baseline length is only suitable for the daytime observations as it does not explain why our nighttime observations have high ratios. Applying the scaling actually exaggerates the situation as it acts to reduce $B_{\rm eff,calc}$, increasing the ratio of $B_{\rm eff,fit}/B_{\rm eff,calc}$, which is already >1 at night. A natural explanation, again following Ishizaki & Sakamoto (2005), is that the measured wind speed as used in $B_{\rm eff,calc}$ is an underestimate of the advecting turbulent phase screen. Those authors do not report any difference between their day and night observations and present the average relationship of phase screen and wind speed, as noted above $v_{\rm screen} = 1.2\ v_{\rm wind}$. That said, they use summer observations in contrast to the generally better winter conditions of our data. There is also scatter between screen and wind speeds in their nighttime observations, which can exceed a factor of 2 for their observations with wind speeds within our data range (∼2–12 m s^{-1}). Nevertheless, in the context of our nighttime observations, the high ratios suggest there is a larger discrepancy between the true turbulent screen speed and the wind speed assumed when calculating $B_{\rm eff,calc}$. Higher ratios than ∼1.2 could also be interpreted as an increased phase screen height compared to that assumed (see also Section 4.3). Using Equation (9) of Ishizaki & Sakamoto (2005) under the caveat of their assumptions, the screen height becomes implausibly large (>400 km) for our lowest wind speed observations and instead likely points to the case where the

Table 7
Ratio of $B_{\rm eff,fit}/B_{\rm eff,calc}$ for the DGC Source

Name	Cycle Time				
	24 s	48 s	72 s	96 s	120 s
Band 7-3					
J2228-170827-B73-1deg	1.34	1.33	1.61	1.53	1.49
J2228-170829-B73-1deg	0.46	0.57	0.51	0.56	0.55
J2228-170829-B73-3deg	1.10	1.01	0.84	0.81	0.71
J2228-170829-B73-6deg	1.12	1.24	1.19	1.24	1.23
J0449-170829-B73-2deg	1.20	1.41	1.48	1.58	1.70
J0449-170829-B73-3deg	1.85	1.78	1.90	1.87	1.94
J2228-170830-B73-1deg	2.42	2.54	2.75	2.81	2.58
J2228-170830-B73-3deg	1.60	1.52	1.90	1.86	2.16
J0449-170830-B73-5deg	4.84	4.74	5.68	5.63	5.42
J0449-170830-B73-7deg	3.64	4.08	4.12	4.31	4.60
J2228-170917-B73-1deg	7.74	6.82	6.02	5.71	5.07
J0633-170917-B73-1deg	0.50	0.44	0.42	0.40	0.35
J0633-170917-B73-4deg	0.55	0.45	0.49	0.45	0.43
J2228-170926-B73-1deg	0.77	1.09	1.56	1.79	1.77
J2228-170926-B73-3deg	1.12	1.48	2.04	2.3	2.58
J2228-170926-B73-6deg	1.78	1.88	1.94	1.98	2.08
J0449-170928-B73-2deg	2.25	2.39	2.58	2.65	2.32
J0449-170929-B73-5deg	0.86	1.01	1.04	1.11	1.05
J0633-170930-B73-1deg	2.95	2.82	2.81	2.75	2.60
J0633-170930-B73-4deg	2.93	2.80	2.79	2.74	2.60
J0633-171001-B73-9deg	2.07	1.73	1.66	1.54	1.42
Band 8-4					
J1709-170717-B84-2deg	1.29	1.30	1.19	1.19	1.11
J1709-170717-B84-1deg	0.63	0.60	0.75	0.73	0.61
J1709-170717-B84-11deg	1.39	1.41	1.95	1.96	1.88
J2228-170717-B84-7deg[a]	1.39	1.55	1.93	2.03	2.28
J1259-170717-B84-1deg	1.39	1.55	1.93	2.03	2.28
J1259-170717-B84-8deg	0.83	0.83	0.94	0.94	1.02
J1259-170718-B84-11deg	0.75	0.76	0.71	0.67	0.52
J0633-170718-B84-1deg	0.52	0.79	0.70	0.76	0.61
J0633-170718-B84-4deg	0.08	0.14	0.16	0.19	0.18
J0633-170718-B84-9deg	0.57	0.76	0.86	0.97	0.96
J0633-170718-B84-6deg	0.42	0.67	0.95	1.16	1.12
J2228-170819-B84-1deg	1.13	1.17	1.40	1.42	1.41
J2228-170820-B84-3deg	2.18	1.93	1.84	1.75	1.65
J2228-170820-B84-10deg	1.87	1.55	1.83	1.69	1.75
J2228-170820-B84-1deg	1.43	1.22	1.45	1.36	1.41
Band 9-4					
J2228- 170717-B94-1deg	0.49	0.54	0.42	0.44	0.35
Band 9-6					
J2228-170725-B96-1deg	1.59	1.53	1.39	1.37	1.18
J2228-170725-B96-6deg	1.39	1.25	1.51	1.45	1.69
J0449-170725-B96-5deg	1.48	1.19	1.40	1.28	1.40
J0449-170725-B96-7deg	0.57	0.84	1.44	1.69	2.11
J0449-170725-B96-12deg	2.86	2.69	2.39	2.33	1.87
J2228-170825-B96-3deg	0.97	1.20	1.14	1.25	1.06
J2228-170828-B96-6deg	1.21	1.39	2.27	2.41	2.69

Note.
[a] Problematic high-phase rms baselines skewing fitting and mean values.

theory of an advecting phase screen breaks down. Even if we consider that the frozen screen approximation is valid, conditions vary diurnally and likely between seasons such that any wind speed measured from the weather masts will require a correction, by some varying factor, in order to estimate the true screen speed.

4.1.4. Can We Rely on the Theoretical Effective Baseline Length?

Overall, one should be cautious in directly using $B_{\rm eff,calc}$ as the proxy for the baseline length at which to extract the phase rms, especially if that phase rms is intended to assess whether observations should be scheduled. In the cases we have examined, where the calibrator separation angle is zero, a factor of 2 difference between $B_{\rm eff,calc}$ and $B_{\rm eff,fit}$ would lead to inaccuracies of $\sim$1.5 in phase rms. This propagates to uncertainties of between 15% and 25% in expected coherence if the actual phase rms was 30° or 50°, respectively, at $B_{\rm eff}$. This is likely a representative conclusion for all observations where the separation angle between a target and calibrator is negligible (see also Section 4.2). Furthermore, theory clearly does not hold for low wind speeds where the ratio can far exceed 2.5. We suggest rather that the phase rms simply be measured directly from a short stability check observation, long enough in time to cover the intended cycle time of the science observation, that would then be used to decide whether or not an observation could take place, rather than relying on an effective baseline-length calculation alone.

4.2. Phase Error Budget—Accounting for Calibrator Separation Angles

In Section 3.3.2 it was seen that the B2B images made with close calibrators improve with reduced cycle times, as phase fluctuations are better corrected. In contrast, the in-band images made with distant calibrators remain with a low and constant coherence irrespective of cycle time. In these cases it is clear that the separation of the phase calibrator is dominating the phase rms error budget, leading to decoherence. The full expression for the effective baseline length to account for calibrator separation is $B_{\rm eff,calc} = v_{\rm wind}t_{\rm cyc}/2 + d$, where d is the physical distance in the troposphere between the calibrator and target (Holdaway & Owen 1995). Recent B2B studies by Asaki et al. (2020b) indicated that d is only $\sim$12 m when considering a phase screen at 500 m height, a target and calibrator horizontal separation angle of 1°, and an observing elevation angle of 45°. In an ideal B2B use case the effect of separation angle should be negligible (see also Maud et al. 2020). For our close calibrator observations with the most distant calibrator at 1.°67, d would be $\sim$20 m when using the same example parameterization. Considering the shortest cycle time, 24 s, and a wind speed of 6 m s^{-1} (without any correction factors as discussed in Section 4.1), $B_{\rm eff,calc} = v_{\rm wind}t_{\rm cyc}/2 + d = 72$ m + 20 m, i.e., dominated by the temporally variable component of the advecting phase screen. The phase rms difference if we account for separation angle is only a factor of $(92/72)^{0.6} = 1.15$ larger for $B_{\rm eff,calc} = 92$ m compared to 72 m (assuming the canonical baseline scaling $b^{0.6}$). If $\sigma_\phi(72\,{\rm m}) = 30°$ then $\sigma_\phi(92\,{\rm m}) = 34.°5$ and therefore the expected coherence would change only $\sim$4% from $\sim$87% to $\sim$83% (consistent with Section 3.1.2 from Maud et al. 2020). The difference diminishes when considering longer cycle times and close calibrators (<1.°67), so one can reasonably assume the separation angle has a generally negligible effect.

To go one step further we investigate the ratio of $d/B_{\rm eff,fit}$ for our data. In Figure 11 we show $d/B_{\rm eff,fit}$, where $B_{\rm eff,fit}$ is the value established in Section 4.1 measured from the DGC source data as a function of separation angle. Light and dark symbols represent the B2B close calibrator and in-band distant calibrator data, respectively. For simplicity we calculate d assuming a phase screen of altitude 1000 ± 500 m, use the

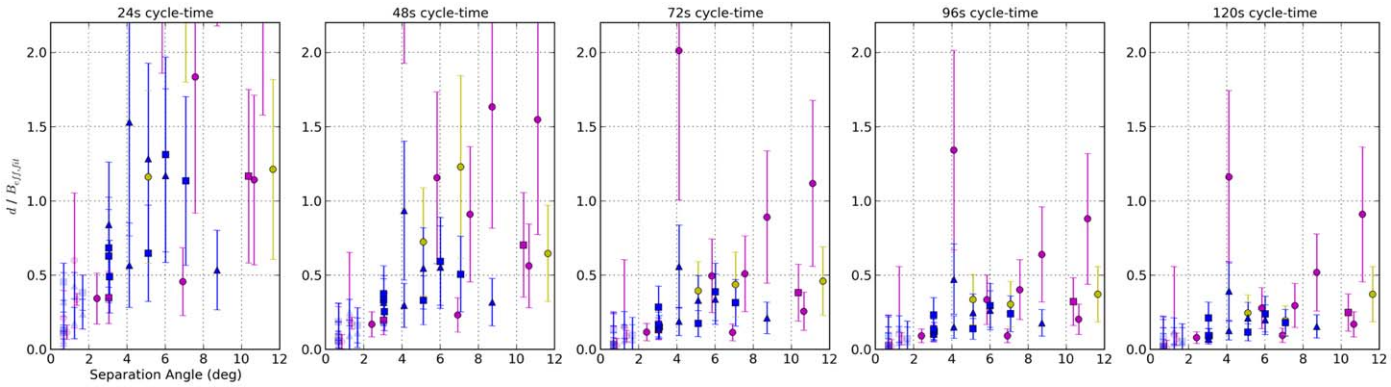

Figure 11. Plot of $d/B_{\rm eff,fit}$ against in-band calibrator to target separation angles for all cycle times 24, 48, 72, 96, and 120 s. $B_{\rm eff,fit}$ is representative of the true value of $v_{\rm wind}t_{\rm cyc}/2$ whereas d parameterizes the effective baseline-length component due to a distant calibrator following Holdaway & Owen (1995). The colors (bands) and symbols (baseline length) follow those in Figure 2 although B2B close calibrator observations are plotted in a lighter shade. For short cycle times, it is evident for separation angles >4°–5° that d is dominant and therefore leads to larger effective baseline lengths and thus a larger phase rms. Fast phase referencing with distant calibrators would therefore not yield an optimal phase calibration as d is unchanged. For the longest cycle time, 120 s, $d/B_{\rm eff,fit}$ is of a similar level to B2B observations, indicating a dominance due to atmospheric variability, hence in-band observations with distant calibrators are most similar to B2B observations with close calibrators only in this case. The uncertainties propagate from the calculation of d using a 1000 ± 500 m altitude atmospheric layer. For 24 s cycle times there are five data sets where $d/B_{\rm eff,fit} > 2.5$ and exceed the plot range.

target source elevation, and assume a horizontal separation between a target and calibrator on the sky. Figure 11 illustrates that when the calibrator to target separation angles are >4°–5°, d, as calculated based on theory often dominates the phase error budget for the shortest cycle time, 24 s. For 48 s cycle times d is typically half as large as the temporally variable component of the phase screen but still notably increases $B_{\rm eff,calc}$. For such fast cycle times the phase calibration will always be suboptimal for larger calibrators to target separation angles because d provides a large or dominating contribution in establishing the phase rms. For longer cycle times, 120 s, $d/B_{\rm eff,fit}$ for distant calibrators reduces to <0.2, closer to the values for B2B data using close calibrators (lighter symbols). Comparing back to Figure 7 (bottom rightmost panel) we saw that the measured in-band image coherence of the targets (using distant calibrators) are comparable with those from the B2B images (using close calibrators) as the long cycle time underpins the phase rms, i.e., the temporally varying phase screen dominates the phase error budget, not d. Of course, the long cycle time data have a notably higher phase rms in that long cycle times have a similar effect to using more distant calibrators, and vice versa. The important message is that fast-switching phase referencing will not better correct temporal atmospheric phase fluctuations when distant phase calibrators are used.

4.3. The Effective Baseline Length with Distant Calibrators

To examine whether the parameterization of $B_{\rm eff,calc} = v_{\rm wind}t_{\rm cyc}/2 + d$ is representative for ALMA observations with distant calibrators, where d is significant, we calculate a scaling factor to increase the phase rms as would be caused due to increasing the effective baseline length by the addition of d. As summarized in Section 4.1.4 we already know that using $B_{\rm eff,calc} = v_{\rm wind}t_{\rm cyc}/2$ alone is not reliable when d is negligible, hence, instead we use $B_{\rm eff,fit}(t_{cyc})$ from Section 4.1 as measured directly from the data (and representative of $v_{\rm wind}t_{\rm cyc}/2$). The phase rms is thereafter scaled up by a factor $= ((B_{\rm eff,fit}(t_{cyc}) + d)/B_{\rm eff,fit}(t_{cyc}))^{\alpha}$, where α is the fitted slope to the uncalibrated SSF. In cases with short cycle times and distant calibrators, d can more than triple the effective baseline length, leading to an increase of the expected phase rms by almost a factor of 2 (i.e., $3^{0.6}$, where $\alpha = 0.6$).

In Figure 12 we plot the measured in-band image coherence for targets calibrated using distant phase calibrators against an estimated coherence, calculated from the scaled expected phase rms for all cycle times when accounting for d (we also correct the expected phase rms to account for the elevation change between the DGC source and the target). We exclude band 9 observations as the image coherence is uncertain considering that we do not truly know the target source fluxes as they were too weak to be self-calibrated. Additionally, for the band 7 long-baseline data, we also account for the effect of the so-called antenna position uncertainties[13] that act to reduce the image coherence. We follow the prescription from Maud et al. (2020) and increase the measured image coherence for the affected data accordingly (over 10% in some cases). Figure 12 highlights that the expected coherence is consistently overestimated for all observations, especially for the shortest cycle times where the effect of d should be the greatest. Only for the longest cycle time, 120 s, does the expected coherence more closely agree with the images, which is when the atmospheric variability dominates the error budget as the contribution to $B_{\rm eff,calc}$ by d becomes negligible. Overall, the theoretical parameterization of d for our observations does not sufficiently increase the effective baseline length and correspondingly does not increase the expected phase rms enough to account for the true loss of image coherence.

Working in reverse, we find that d ought to be a few to tens times larger than calculated to achieve a sufficient phase rms scaling for the estimated and image coherence values to agree. Considering the parameterization of d, the only variable that we assume could be responsible is the atmospheric screen height, which is required to be of the order of thousands of meters to increase d sufficiently. Interestingly, half of the required screen height values range between 4000 and 8000 m, and the rest are

[13] The antenna positions are not uncertain due to physical position changes, the uncertainties are caused by unmodeled variations in the path length above each antenna during the observations. Comparisons of antenna positions from a number of all-sky-delay observations (Hunter et al. 2016) change due to a changing troposphere, most likely affecting the zenith path delay component that varies on timescales of many hours to days.

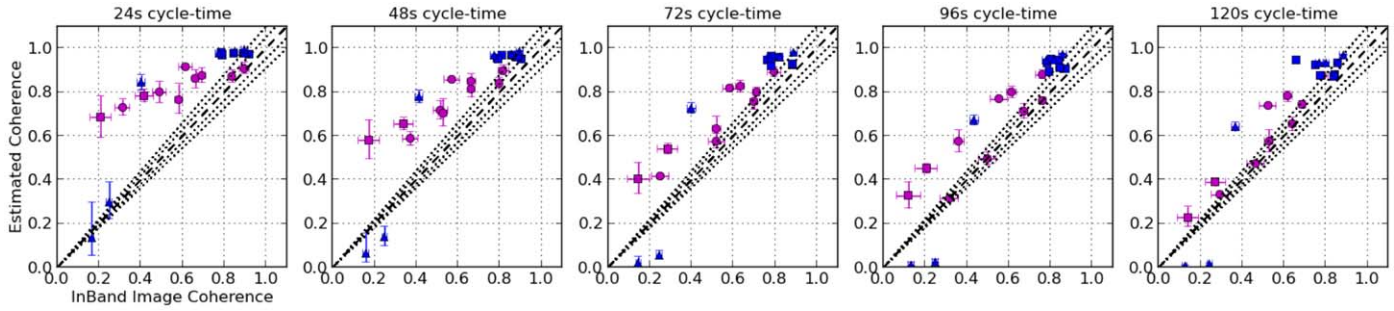

Figure 12. Plots of the measured in-band image coherence for targets calibrated using distant phase calibrators against the estimated coherence, as calculated from the scaled expected phase rms for all cycle times (24, 48, 72, 96, and 120 s from left to right) to account for d via the theoretical parameterization. We exclude band 9 observations as the image coherence is uncertain. For the band 7 long-baseline data, we correct the image coherence due to the so-called antenna position uncertainties. The colors (bands) and symbols (baseline length) follow those in Figure 2 while errors in image coherence are propagated from an uncertainty in the peak flux density of three times the image noise level, and those in expected coherence propagate from using lower and upper limits of 500 and 1500 m for the screen height in the calculation of d. The main result is that for the shortest cycle times, 24–72 s, the expected coherence is considerably overestimated, i.e., the effective baseline lengths are underestimated. The reason is that the addition of d does not sufficiently increase the effective baseline length and thus the expected phase rms is underestimated. For the longest cycle time, 120 s, the effect of d is almost insignificant (see Figure 11), and the estimated and measured image coherences values are coincident.

below this, except two, which are >15 km. This is counter to ALMA site tests that suggest the turbulent screen height is likely <1000 m (Robson et al. 2001). Large screen heights have been previously been reported in ALMA phase-referencing and phase metrics studies (Asaki et al. 2016; Matsushita et al. 2017). Specifically, in excellent conditions with both low PWV and a low phase rms, the atmospheric variations are likely dominated by a dry component, not by the typically dominant water vapor content in the turbulent layer (e.g., Stirling et al. 2005). Long-baseline observations with no apparent turnover in the SSF (Matsushita et al. 2017) point to screen heights >10 km. We have only two nighttime observations where the estimated screen height is ∼15 km, and although these data do not show a sharp turnover in the SSF, neither do they have a single continuous slope when compared with data presented in Figure 2 of Matsushita et al. (2017). A higher phase screen also corroborates the earlier discussion in Section 4.1 where we indicated that high ratios of $B_{\rm eff,fit}/B_{\rm eff,calc}$ (where d was zero) for nighttime observations could be due to screen and wind speed discrepancies caused by a variable (higher) screen height. We do not, however, find any statistically significant trend between $B_{\rm eff,fit}/B_{\rm eff,calc}$ and the estimated required screen heights.

Simulation work (e.g., Holdaway et al. 2004, and references therein) points to low (500–1000 m) phase screens that likely tie with water-vapor-dominated conditions, unlike our mostly low-PWV data, while phase screen investigations by Ishizaki & Sakamoto (2005) only use short baselines aligned with the dominant wind direction, east to west. Hence, for our data, and for real ALMA high-frequency observations using a complex antenna distribution and extended array configuration, the parameterization of $B_{\rm eff,calc}$, accounting for d as forecast from simulations, is insufficient in encompassing the real-world negative effects of distant calibrators.

4.3.1. A Note on Short-baseline Observations

For short-baseline observations (<500 m) in cases where $B_{\rm eff,calc} > B_{\rm max}$, regardless of accounting for d, phase referencing does not correct for the temporal atmospheric variations (this is was already explained decades ago by Masson 1994) and so distant calibrators should, in theory, not lead to any increase in the phase rms. The phase rms is limited in such cases by the atmospheric stability of the longest baseline of the array—which are a few hundred meters at most. However, large separation angles (>10°–15°) should be avoided in case they are big enough to cause phase offsets as introduced by antenna position uncertainties (Maud et al. 2020), or intrinsic offsets due to absolute phase differences at different sky locations. In cases where sufficiently fast switching is used, such that $B_{\rm eff,calc} < B_{\rm max}$ (<32 s for the shortest ALMA array with $B_{\rm max}$ = 160 m, assuming a 10 m s^{-1} wind speed and without including d), our above analysis would hold, i.e., theory would underestimate $B_{\rm eff,calc}$ and the phase rms remaining in the data, and hence would provide an expected coherence larger than can be achieved in reality. Overall, the use of fast switching would not significantly improve the phase rms for short-baseline observations, because the phase rms is intrinsically lower as compared with much longer baselines (>1000 m), and the observations would simply be inefficient.

4.4. Estimating the Coherence

Considering the above analysis in Section 4.3, the theoretical parameterization of effective baseline length while accounting for the calibrator separation angle through d and the subsequent estimate of phase rms is not sufficiently accurate in providing an estimate of the achievable coherence. Instead, we consider the empirical formulation presented in Maud et al. (2020), who fitted the degradation of image coherence as a function of calibrator separation angle for a subset of observations that should have achieved a low phase rms (<30°) and that used fast cycle times (24 s). Grouping the observations by visibility baseline length, separated into short and long below and above 5×10^6 kλ, the coherence degradation as a function of separation angle (θ) is as follows: -0.022 ± 0.005 and -0.054 ± 0.012 per degree, respectively. This loss of coherence is in addition to that caused by the atmospheric variability (which as we detail in Section 3.1 is a function of time).

In Figure 13 we plot in-band image coherence for targets calibrated using both close and distant phase calibrators compared with the empirically estimated coherence. The coherence estimate uses the measured phase rms on the DGC as a function of cycle time (correcting also for the DGC source and target elevation difference) and is reduced further by the coherence degradation as a function of separation angle from Maud et al. (2020). Compared with Figure 12, here we see a much better agreement between the estimated and image

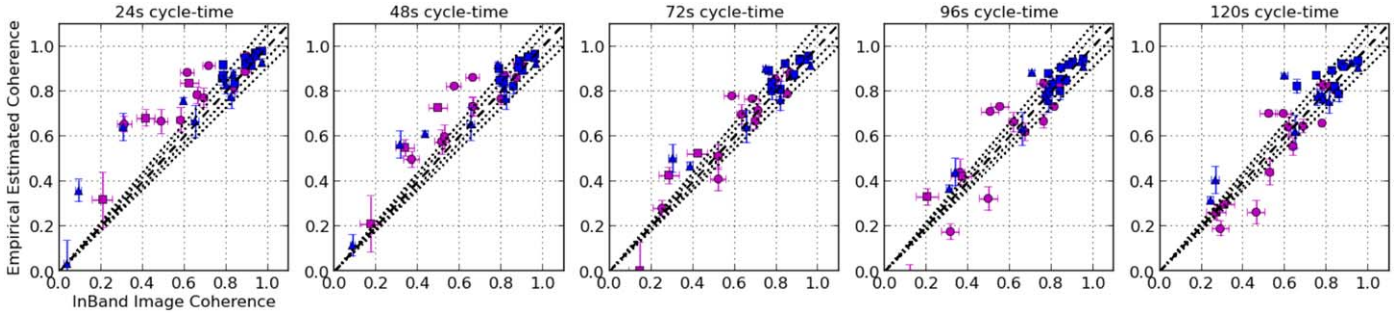

Figure 13. Plots of the measured in-band image coherence for targets calibrated using both close and distant phase calibrators against the empirically estimated coherence calculated using the estimated phase rms (over all cycle times, 24, 48, 72, 96, and 120 s from left to right) and while also accounting for any further coherence degradation due to calibrator to target separation angles as parameterized in Maud et al. (2020). Compared to Figure 12, here the empirical estimated coherence is more consistent with the image coherence for all cycle times, and thus the empirical method is better to use as a proxy for estimating what the image would likely achieve. Some estimated coherence values can be unphysical, <0, as the reduction in coherence when accounting for the target to calibrator separation angles is a simple subtraction—this happens only for very high phase rms, poor conditions. The colors (bands) and symbols (baseline length) follow those in Figure 2 while errors in image coherence are propagated from an uncertainty in the peak flux density of three times the image noise level and those in empirical expected coherence are propagated using the lower and upper limits of the degradation of coherence as a function of separation angle.

coherence values for all cycle times, and in particular for data sets where the achieved coherence is >70%, which agree to within 10%–15%. We caution that the subset of data used to study the coherence degradation with separation angle derived by Maud et al. (2020) is part of the same data we present here, and thus a deep examination of previous ALMA archive data and more testing data would be beneficial in confirming this proposed methodology.

4.5. Optimizing ALMA Observations

From Section 4.4, the measured atmospheric variability combined with the parameterization of coherence degradation with calibrator separation angle appears to be sufficiently accurate to provide insight into an observing strategy, both in terms of whether to observe (or not) and what optimal cycle time to use. Although ALMA already implements a number of phase stability assessments, which include PWV monitoring and use of the WVR system to predict the phase correction based on previous observations, a measure of the phase stability from the bandpass and phase calibrator solutions from the immediately preceding observational data, active monitoring of the solutions from point sources during the observations, and the ability to run (at the discretion of the astronomer on duty) a short observation targeting a point-source calibrator to measure the two-minute timescale phase rms (a stability check observation); the observing cycle times are fixed. The current ALMA phase stability measures are used only to decide whether to observe or not. To further optimize ALMA observations, dynamic adjustment of the observing strategy, such as cycle times and calibrator on-source times, need to be implemented. We have clearly demonstrated that faster cycle times combined with close phase calibrators can significantly improve image coherence and thus offer more opportunities to observe in conditions traditionally classified as too poor, especially at higher frequencies. A dynamic system could be employed to exploit rare low-PWV observing nights where high-frequency observation could take place but when the phase rms would otherwise have been categorized as too unstable with the ALMA's current fixed cycle time regime. There are however a number of considerations, such as, the shortest permitted cycle time values and the impact on efficiency that must be accounted for and investigated in detail before a dynamic system could be implemented.

Below we provide a simple pragmatic approach for a future dynamic cycle time method based on our findings in this work and those previously presented in Maud et al. (2020). Such an approach could be implemented using a refined phase stability assessment while incorporating limits for permitted decoherence and observing efficiency. Focusing specifically on the refinement of long-baseline observations, we are interested in timescales less than 2 minutes. Using either the bandpass source scan, from a previous science project, or preferably using a dedicated 2 minute phase stability observation immediately before beginning the science observation in question, the phase rms as a function of time could be assessed (as in Section 3.1). The optimal cycle time ($t_{\rm dyn}$) can then already be easily constrained via

$$t_{\rm dyn} = \left(\frac{\sigma_{\phi,\rm tdyn}}{\sigma_{\phi,\rm tcyc}}\right)^{1/n} t_{\rm cyc}, \quad (5)$$

where n is the power-law change of phase rms as a function of time ($n \sim 0.5$ on average in Section 3.1, i.e., phase rms varies as $\sqrt{\rm time}$, but n could be measured over the 2 minute stability check), $t_{\rm cyc}$ is the default observing cycle time, $\sigma_{\phi,\rm tcyc}$ is the phase rms for the default cycle time (in radians) as is calculable from the stability check observation, and $\sigma_{\phi,\rm tdyn}$ is

$$\sigma_{\phi,\rm tdyn} = \sqrt{-2\ln\left(V_{\rm lim} - m\theta\right)}, \quad (6)$$

where $V_{\rm lim}$ is our input acceptable lower limit for the coherence of the observation we wish to conduct, θ is the target to calibrator separation angle, and m is the gradient selected from Table 8 presented in Maud et al. (2020), which is negative (as also reported in Section 4.4) and governs the loss of coherence as a function of calibrator separation angle (combining antenna position uncertainties and suboptimal phase referencing). When using B2B calibration, the acceptable lower limit for coherence should be larger to account for slight coherence losses due to the addition of the DGC step. The impact of DGC can also be estimated using the phase stability assessment provided that the DGC cycle time is known. Using the equation presented in Section 3.1.1 of Maud et al. (2020), we parameterize the B2B

coherence limit, $\boldsymbol{V}$ lim,B2B as

$$\boldsymbol{V}\,\mathrm{lim,B2B} = \boldsymbol{V}\,\mathrm{lim} + 0.179\log_{10}(57.3 \times \sigma_{\phi,\mathrm{DGC}}) - 0.194, \quad (7)$$

where $\sigma_{\phi,\mathrm{DGC}}$ is the phase rms expected for the DGC source in radians for the given DGC cycle time. For $\sigma_{\phi,\mathrm{DGC}} < 20^\circ$ (0.35 rad) the DGC steps typically reduce image coherence by <4%.

Having calculated t_{dyn} via Equation (6), a final assessment would be to account for the observational efficiency when referring to a predefined efficiency limit. One could use either the target and phase calibrator duty-cycle directly, or as proposed by Holdaway (2001), the square root of the duty cycle such that the time efficiency is $\varepsilon_t = \sqrt{t_{\mathrm{tar}}/t_{\mathrm{dyn}}}$, where t_{tar} is the on-target time. Establishing an efficiency limit is however not an easy task and must consider effects on the schedule and observing queue and a careful weighting of likely available weather conditions, which requires a statistical study of conditions at Chajnantor. One additional dilemma for the reader to consider is whether to prioritize making a long-baseline band 9 observation that is knowingly less efficient compared to a band 6 or band 7 one, while balancing, in the best case, that the PWV is only low enough ∼20%–25% of the time (in July and August) to use band 9, while typically band 6 or band 7 could be done essentially ∼77% of the time (excluding low atmospheric transmission frequencies within those bands). We therefore avoid any discussion of a fixed efficiency limit but rather provide a comparative scenario below.

To provide an illustrative worked example and to show how dynamic calibrator on-source times can also help with efficiency we consider a long-baseline band 7 observation. Such observations have $t_{\mathrm{cyc}} = 78$ s (18 s calibrator and 54 s target) when accounting for 3 s of slew for each change to and from the target and results in a duty cycle, $t_{\mathrm{tar}}/t_{\mathrm{cyc}}$, of 69.2%, or ε_t of 0.83 (as a fraction).

Maud et al. (2020) suggest that images with a coherence loss of >30% generally begin to have structure defects (see also Carilli & Holdaway 1999), while Perley (1999) detail the significant effect of phase errors on image dynamic range, as is also explored by Martí-Vidal et al. (2010b) at centimeter wavelengths. Thus, a sensible coherence limit, $\boldsymbol{V}_{\mathrm{lim}}$, for this example would be 0.7. Assume we conducted a 2 minute stability check observation and found that the phase rms increases with $\sqrt{\mathrm{time}}$ ($n = 0.5$ in Equation (5), as in Section 3.1) and that $\sigma_{\phi,\mathrm{tcyc}}$ is 40°. The atmospheric phase rms alone suggests a coherence of 0.78 would be achievable for the default cycle time, however, the phase calibrator in this example is 3° away from the target reducing the coherence by a further 0.16. Hence, for the 78 s cycle time observation, an expected coherence of 0.62 would be considered as unacceptable. In order to optimize this observation we find that $\sigma_{\phi,\mathrm{tdyn}}$ should be ∼31° from Equation (6), which results in a refined cycle time t_{dyn} of 44 s from Equation (5).

Considering the previous calibrator and slew times per cycle time, of 18 s and 6 s, respectively, the on-target time would reduce to 20 s. The duty cycle would thereby drop to 45% ($\varepsilon_t = 0.67$), which is notable. If a strong phase calibrator is used we could make a further refinement and reduce the scan time to 8 or 12 s, for example, assuming that a sufficient S/N ratio would still be achieved. In the case of phase referencing using B2B for high-frequency observations, the phase calibrators observed at a lower frequency would often be notably stronger. With shorter calibrator scans, the target source would get 10 or 6 s more on-source time per cycle time, and the duty cycle and efficiency would increase to 68.2% ($\varepsilon_t = 0.83$) and 59.1% ($\varepsilon_t = 0.77$) respectively. This hypothetical situation using a 44 s cycle time, where 8 s is on the calibrator, 6 s is slew time, and 30 s is on the target, achieves almost exactly the same efficiency as the original 78 s scenario but crucially obtains a higher final image coherence.

Moreover, we assume that a closer calibrator could be found when using the B2B observing mode, which is much more likely compared to an in-band observation when using such short on-calibrator times (Asaki et al. 2020a) and so we can further improve the efficiency. First we must formulate $\boldsymbol{V}_{\mathrm{lim,B2B}}$ to account for the DGC step. Assuming the DGC cycle time is 24 s and, as above, the stability check found $\sigma_{\phi,\mathrm{tcyc}} = 40^\circ$ over 78 s, then $\sigma_{\phi,\mathrm{DGC}}$ is ∼20°. Hence, the DGC would cause a 3.8% coherence loss, and via Equation (7) we find $\boldsymbol{V}_{\mathrm{lim,B2B}} = 0.738$. Using $\boldsymbol{V}_{\mathrm{lim,B2B}}$ in Equation (6) and now considering a closer calibrator at $\theta = 1^\circ$ (empirically only a 0.054 loss of coherence) we find that $\sigma_{\phi,\mathrm{tdyn}}$ should be ∼39°. This means the dynamic cycle time, via Equation (5), is actually only marginally reduced to 77 s from the original 78 s, and notably longer than the above 44 s (for the in-band example) because the close calibrator has very little impact on the coherence. Finally, using this 77 s cycle time, 8 s on the calibrator, and 6 s slew time, we have 63 s on-source time for the target per cycle time. Thus, a higher efficiency in terms of the duty cycle $t_{\mathrm{tar}}/t_{\mathrm{cyc}} = 81.8\%$, or ε_t of 0.90, is achieved for the B2B mode using a 1° separated calibrator compared to the in-band case with the calibrator at 3°.

5. Summary

We have analyzed 44 data sets taken as part of the ALMA high-frequency long-baseline campaign 2017 (HF-LBC-2017) and made comparisons between the standard, in-band phase-referencing, and B2B phase-referencing techniques for a range of phase-referencing cycle times. We analyzed in detail how the phase rms changes with timescale using the DGC source. The changes of target image coherence as a function of cycle time for in-band and B2B calibrated data, while also considering the use of close (<1.°67) and distant (2.°4–11.°7) phase calibrators, were also investigated. We made an assessment of the accuracy of the theoretical parameterization of the effective baseline length and its use for estimating the phase rms and thereafter the expected image coherence of phase-referenced data. This was compared to an empirical parameterization for the estimated coherence. A possible methodology to optimize ALMA observations using dynamic cycle times and on-calibration times was also examined.

Our investigation using the DGC source data, after correction with the ALMA WVR system, shows that the estimated phase rms increases, on average, as a function of $\sqrt{\mathrm{time}}$ ($t^{0.52\pm0.09}$), provided only the longer baselines are considered in the phase rms calculation. Assuming a moving atmospheric phase screen above the array, all baselines over 1500 m conform to this criteria for our observations, using the longest cycle time of 120 s and a maximal wind speed of ∼12 m s^{-1}. We find that the expected coherence, calculated using either the expected or residual phase rms, and the image coherence of the DGC source are coincident within 5%−10%.

For in-band and B2B data calibrated with close phase calibrators, we find that the image coherence degrades as a

function of increasing cycle time, closely following that expected when considering the atmospheric variability (phase rms as a function of time). Faster cycle times can notably improve the phase calibration and therefore the resultant image coherence, provided close phase calibrators are used. The coherence improvement is diminishing for decreasing phase rms as images already have high coherence values >87% for low phase rms values <30°. On the contrary, when using distant phase calibrators the image coherence is largely unchanged as a function of cycle time. The achievable image coherence of target sources is dominated by the use of a distant calibrator that does not act to reduce the phase rms, irrespective of the cycle time, after phase referencing. The effect of using distant phase calibrators is the same as using the long cycle times with close calibrators, the phase rms is the largest in both scenarios, and consequently the images have the lowest coherence. Fast phase referencing with distant phase calibrators will not improve calibration or target image coherence.

The theoretical effective baseline length, the baseline length after which the phase rms should be constant after calibration using a cycle time of $t_{\rm cyc}$ and parameterized by $B_{\rm eff,calc} = v_{\rm wind}t_{\rm cyc}/2 + d$, is within a factor of 2 of the value measured directly from the observations in cases where the calibrator separation angle component, d, is negligible. The factor of 2 results in 15% and 25% estimated coherence inaccuracies if the phase rms is 30° and 50°, respectively, at the effective baseline length. In comparing the atmospheric, $v_{\rm wind}t_{\rm cyc}/2$, and calibrator distance, d, components of the effective baseline length, we show that for our observations using distant calibrators the phase error budget is significantly increased or dominated by d. In some cases the addition of d doubles the phase rms value. However, even when accounting for d, the total effective baseline length is underestimated, resulting in an underestimated phase rms that consequently leads to an overestimated expected coherence when compared with what is measured from the images. The coherence in the images can be more than 0.2 (20%) lower than expected. The theoretical parameterization is therefore unsuitable in accurately estimating the achievable image coherence.

Combining a previously established empirical trend of image coherence degradation as a function of the calibrator to target separation angle with the measured atmospheric variability via the expected phase rms, we are much more accurately able to estimate the expected image coherence. For observations with an image coherence of >0.7, irrespective of calibrator separation angle, the estimated coherence was typically within 10%–15% of that achieved in final images. Using this method to establish the expected coherence, we examined a pragmatic approach to optimize ALMA observations by reducing the cycle time as required to achieve a preestablished coherence limit. Provided the updated (shorter) cycle time does not reduce efficiency below an observatory set limit, an observation could take place rather than being avoided as conditions would have traditionally been classified as too poor. In addition, and especially for the B2B mode, shorter phase calibrator scan times and closer calibrators could be used. When combined, shorter cycle times and short phase calibrator scan lengths can yield a similar or even improved efficiency, compare to in-band observations with slower cycle times and long phase calibrator scan times.

ALMA is a partnership of ESO (representing its member states), NSF (USA) and NINS (Japan), together with NRC (Canada) and NSC and ASIAA (Taiwan), and KASI (Republic of Korea), in cooperation with the Republic of Chile. The Joint ALMA Observatory is operated by ESO, AUI/NRAO, and NAOJ. We would also like to thank all the Joint ALMA Observatory staff in Chile for performing the challenging HF-LBC-2017 successfully, and specifically Eric Villard as EOC lead during the testing. L.T.M. was adopted as a JAO ALMA expert visitor during his stays at JAO during the campaign. This work was supported by JSPS KAKENHI grant No. JP16K05306. S.M. is supported by the Ministry of Science and Technology (MOST) in Taiwan, MOST 107-2119-M-001-020 and MOST 108-2112-M-001-048.

ORCID iDs

Luke T. Maud https://orcid.org/0000-0002-7675-3565
Yoshiharu Asaki https://orcid.org/0000-0002-0976-4010
Akihiko Hirota https://orcid.org/0000-0002-0465-5421
Edward B. Fomalont https://orcid.org/0000-0002-9036-2747
Satoko Takahashi https://orcid.org/0000-0002-7287-4343
Satoki Matsushita https://orcid.org/0000-0002-2127-7880
Tsuyoshi Sawada https://orcid.org/0000-0002-0588-5595
John Carpenter https://orcid.org/0000-0003-2251-0602

References

ALMA Partnership, Brogan, C. L., Pérez, L. M., et al. 2015a, ApJL, 808, L3
ALMA Partnership, Fomalont, E. B., Vlahakis, C., et al. 2015d, ApJL, 808, L1
ALMA Partnership, Hunter, T. R., Kneissl, R., et al. 2015b, ApJL, 808, L2
ALMA Partnership, Vlahakis, C., Hunter, T. R., et al. 2015c, ApJL, 808, L4
Asaki, Y., Matsushita, S., Kawabe, R., et al. 2014, Proc. SPIE, 9145, 91454K
Asaki, Y., Matsushita, S., Fomalont, E. B., et al. 2016, Proc. SPIE, 9906, 99065U
Asaki, Y., Maud, L. T., Fomalont, E. B., et al. 2020a, ApJS, 247, 23
Asaki, Y., Maud, L. T., Fomalont, E. B., et al. 2020b, AJ, 160, 59
Asaki, Y., Saito, M., Kawabe, R., Morita, K.-I., & Sasao, T. 1996, RaSc, 31, 1615
Briggs, D. S. 1995, BAAS, 27, 112.02
Brogan, C. L., Hunter, T. R., & Fomalont, E. B. 2018, arXiv:1805.05266
Bulter, B. J., Sakamoto, S., & Kohno, K. 2001, ALMA Memo, 365, http://library.nrao.edu/alma.shtml
Carilli, C. L., & Holdaway, M. A. 1997, VLA Memo, 173, http://library.nrao.edu/alma.shtml
Carilli, C. L., & Holdaway, M. A. 1999, RaSc, 34, 817
Cornwell, T. J., & Wilkinson, P. N. 1981, MNRAS, 196, 1067
Coulman, C. E. 1990, in URSI/IAU Symp. on Radio Astronomical Seeing, ed. J. E. Baldwin & S. Wang (Beijing/Oxford: International Academic Publishers/Pergamon Press), 11
Dodson, R., & Rioja, M. J. 2009, arXiv:0910.1159
Holdaway, M. A. 1992, ALMA Memo, 84, http://library.nrao.edu/alma.shtml
Holdaway, M. A. 2001, ALMA Memo, 403, http://library.nrao.edu/alma.shtml
Holdaway, M. A., Carilli, C., & Laing, R. 2004, ALMA Memo, 493, http://library.nrao.edu/alma.shtml
Holdaway, M. A., & Owen, F. N. 1995, ALMA Memo, 126, http://library.nrao.edu/alma.shtml
Hunter, T. R., Lucas, R., Broguière, D., et al. 2016, Proc. SPIE, 9914, 99142L
Ishizaki, H., & Sakamoto, S. 2005, ALMA Memo, 529, http://library.nrao.edu/alma.shtml
Lal, D. V., Matsushita, S., & Lim, J. 2007, arXiv:0706.0149
Lay, O. P. 1997, A&AS, 122, 535
Mangum, J. G., Baars, J. W. M., Greve, A., et al. 2006, PASP, 118, 1257
Martí-Vidal, I., Guirado, J. C., Jiménez-Monferrer, S., & Marcaide, J. M. 2010a, A&A, 517, A70
Martí-Vidal, I., Ros, E., Pérez-Torres, M. A., et al. 2010b, A&A, 515, A53
Masson, C. R. 1994, in ASP Conf. Ser., 59, IAU Colloq. 140: Astronomy with Millimeter and Submillimeter Wave Interferometry, ed. M. Ishiguro & J. Welch (San Francisco, CA: ASP), 87
Matsushita, S., Asaki, Y., Fomalont, E. B., et al. 2017, PASP, 129, 035004

Maud, L. T., Tilanus, R. P. J., van Kempen, T. A., et al. 2017, A&A, 605, A121
Maud, L. T., Asaki, Y., Fomalont, E. B., et al. 2020, ApJS, 250, 18
McMullin, J. P., Waters, B., Schiebel, D., Young, W., & Golap, K. 2007, in ASP Conf. Ser., 376, Astronomical Data Analysis Software and Systems XVI, ed. R. A. Shaw, F. Hill, & D. J. Bell (San Francisco, CA: ASP), 127
Morita, K. I., Handa, K., Asaki, Y., et al. 2000, in ASP Conf. Ser., 217, Fast Switching Experiments with the Nobeyama Millimeter Array, ed. J. G. Mangum & S. J. E. Radford (San Francisco, CA: ASP), 340
Morris, K. 2014, Master's Thesis, NRAO
Perley, R. A. 1999, in ASP Conf. Ser., 180, Synthesis Imaging in Radio Astronomy II, ed. G. B. Taylor, C. L. Carilli, & R. A. Perley (San Francisco, CA: ASP), 275
Petry, D., Stanke, T., Biggs, A., et al. 2020, Msngr, 181, 16
Rampini, F., Marchiori, G., Biasi, R., Stanghellini, S., & Ghedin, L. 2010, Proc. SPIE, 7733, 773314
Rioja, M., & Dodson, R. 2011, AJ, 141, 114
Rioja, M. J., Dodson, R., Jung, T., & Sohn, B. W. 2015, AJ, 150, 202
Robson, Y., Hills, R. E., Richer, J., et al. 2001, ALMA Memo, 345, http://library.nrao.edu/alma.shtml
Sramek, R. A. 1990, in URSI/IAU Symp. on Radio Astronomical Seeing, ed. J. E. Baldwin & S. Wang (Beijing/Oxford: International Academic Publishers/Pergamon Press), 21
Stirling, A., Richer, J. S., Hills, R. E., & Lock, A. 2005, ALMA Memo, 517, http://library.nrao.edu/alma.shtml
Tatarski, V. I., Silverman, R. A., & Chako, N. 1961, PhT, 14, 46
Taylor, G. I. 1938, RSPSA, 164, 476
Thompson, A. R., Moran, J. M., & Swenson, G. W. 2017, Interferometry and Synthesis in Radio Astronomy (3rd ed.; Cham: Springer)
Woody, D., Holdaway, M. A., Lay, O., et al. 1995, ALMA Memo, 144, http://library.nrao.edu/alma.shtml
Wright, M. C. H. 1996, PASP, 108, 520